NANOELECTROMECHANICAL MEMBRANES FOR MULTIMODE MASS SPECTROMETRY

Senior Thesis by

Jarvis Li

In Partial Fulfillment of the Requirements for the Degree of

Bachelors of Science in Physics

California Institute of Technology
Pasadena, California

2014

(Defended May 23, 2014)

© 2014

Jarvis Li

All Rights Reserved

Acknowledgements

First and foremost I would like to thank my research and academic advisor, Professor Michael Roukes for his guidance and support over the last year. I first started working in his group as a SURF student in the summer of 2013 and stayed on for my senior thesis. I am extremely grateful for his help with guiding the research and providing useful tips and ideas to try out after each meeting. I also want to thank my research co-mentor, graduate student Peter Hung for teaching me many tools of experimental physics and for working side by side with me in the lab, spending countless night in a subbasement, but still making it an enjoyable experience. I would also like to thank the rest of the Roukes group for their support, especially Dr. Warren Fon, Caryn Bullard, and Dr. Scott Kelber for their help with experimental work and guidance. I am also grateful for Derrick Chi in helping fabricate new devices. I also want to thank a few former members of the group, Dr. Rassul Karabalin, Dr. Ed Myers, and Dr. Selim Hanay for their expertise and help with experimental techniques and NEMS systems.

Abstract

Nanoelectromechanical systems (NEMS) represent the next wave in miniaturizing various electrical and mechanical devices used in a variety of fields, such as physics, biology, and engineering. In particular, NEMS devices have high surface area to volume ratios, low power consumption, low mass, and extremely small footprints. These properties allow NEMS to explore more fundamental regimes of matter. Current NEMS mass spectrometry advancements have only utilized doubly-clamped beams and cantilevers. However to expand the measurement capabilities of NEMS mass spectrometry, we utilize a circular membrane geometry in order to build upon the existing measurements in 1 spatial dimension to measure mass spatially in 2-dimensions. Furthermore, membranes should provide a larger potential mass dynamic range. For this experiment, we utilize circular piezoelectric membranes of aluminum nitride and molybdenum stacks. For mass deposition, we utilize a technique known as matrix-assisted laser desorption/ionization (MALDI), which focuses a pulsed UV laser onto the desired sample embedded in a corresponding matrix. The energy causes a plume of particles to desorb off the sample and towards the device. As a particle lands on the device, we are able to deduce its mass from the shift in its resonant frequency. In particular we need to measure the first three resonant frequencies, since the frequency shifts also depend on the location the particle landed on the device. Here we show the viability of our detection setup, mass deposition setup, and our mass deposition results.

Table of Contents

Acknowledgements ……………………………………………………………………………v

Abstract ………………………………………………………………………………………vii

Table of Contents ……………………………………………………………………………ix

List of Figures ………………………………………………………………………………xi

List of Tables……………………………………………………………………………...xii

Abbreviations ………………………………………………………………………………xiii

Chapter 1: Introduction .....……………………………………………………………………1

1.1 Background and Motivation for Mass Spectrometry ……………….…………………1

1.2 Background of Nanoelectromechanical Systems………………………………………2

1.3 NEMS Mass Spectrometry ……………………………………………………………3

Chapter 2: Circular Membrane Mass Spectrometry ………………………………………..5

2.1 Mode Shapes …………………………………………………………………………...5

2.2 Multimode Theory ……………………………………………………………………..9

2.3 Allan Deviation ………………………………………………………………………13

2.4 Dynamic Mass Range ………………………………………………………………15

Chapter 3: AlN Device Structure and Operation ……………………………………………17

3.1 AlN (Aluminum Nitride) Properties …………………………………………...17

3.2 AlN Membrane Device Structure ……………………………………………..17

3.3 Overview of Fabrication Procedure ……………………………………………...19

3.4 Actuation Techniques ………………………………………………………………20

3.5 Detection Schemes …………………………………………………………………22

Chapter 4: AlN Device Characterization and Measurements…………………………………...23

4.1 Optical Detection Measurements…………………………………………………...23

4.2 Spatial Response Scan ……………………………………………………………...25

4.3 Frequency Sweeps ……………………………………………………………………29

4.4 Piezoelectric Detection Measurements ………………………………………………32

Chapter 5: Mass Spectrometry Experimental Setup ………………………………………………35

5.1 Optical/Mass Deposition Setup ………………………………………………………35

5.2 Phase Locked-Loop Setup ……………………………………………………………37

5.3 Mass Sample Preparation …………………………………………………………..39

5.4. Mass Deposition Results …………………………………………………………..40

Chapter 6: Conclusion ……………………………………………………………………………47

Bibliography ……………………………………………………………………………………...49

List of Figures

Figure 2.1: Bessel Function Roots for radial modes ……………………………………………..6

Figure 2.2: Bessel Function Roots for azimuthal ………………………………………………...7

Figure 2.3: Plots and Simulations of Mode Shapes ……………………………………………...8

Figure 2.4: Simulation Data for Mass Loading……………………………………………………12

Figure 2.5: Allan Deviation for Individual and Concurrent Measurements………………………14

Figure 3.1: AlN Membrane Device Structure and SEM Images………………………………..19

Figure 3.2: Piezoelectric Actuation Scheme………………………………………………………21

Figure 4.1: Optical Detection Experimental Setup ………………………………………………..23

Figure 4.2: Sample Chamber ……………………………………………………………………24

Figure 4.3: 3D Scan of 01 Mode ………………………………………………………………….26

Figure 4.4: 3D Scan of 11 Degenerate Modes…………………………………………………….28

Figure 4.5: Frequency Sweeps of 01 Mode ……………………………………………………….30

Figure 4.6: Frequency Sweeps of 11 Mode ……………………………………………………….32

Figure 4.7: Piezoelectric Detection Frequency Sweep ……………………………………………32

Figure 5.1: Schematic of Mass Deposition Coupled with Optical Detection Setup ………………36

Figure 5.2: Phase-locked Loop Circuit Diagram ………………………………………………….38

Figure 5.3: Gold Nanoparticle Sample Slide ……………………………………………………...39

Figure 5.4: One Mode PLL Tracking Data with Mass Loading ………………………………..41

Figure 5.5 SEM Images of Gold Nanoparticle Deposition on Device……………………………42

Figure 5.6: EDX Data from Gold Nanoparticle Deposition ………………………………………43

Figure 5.7: Three Mode PLL Tracking with Mass Loading………………………………………44

List of Tables

Table 2.1: Constants for Mode Shape Equations ………………………………………………………..8

Table 2.2: Effective Mass Correction Constants………………………………………………………..10

Table 5.1: EDX Energy Levels……………………………………………………………………43

Abbreviations

AC – Alternating Current
AFM – Atomic Force Microscopy
AlN – Aluminum Nitride
Da – Dalton
DI – Deionized
EDX – Energy Dispersive X-ray Spectroscopy
ESI – Electrospray Ionization
GNP – Gold Nanoparticles
GPIB – General Purpose Interface Bus
HF – Hydrofluoric Acid
ICs – Integrated Circuits
MALDI – Matrix Assisted Laser Desorption Ionization
Mo – Molybdenum
MS – Mass Spectrometry
NA – Network Analyzer
NEMS – Nanoelectromechanical Systems
PLL – Phase-locked Loop
Q – Quality Factor
SEM – Scanning Electron Microscope
Si – Silicon
SiO_2 – Silicon Dioxide
USB – Universal Serial Bus
UV – Ultraviolet
VCO – Voltage Controlled Oscillator

Chapter 1

Introduction

1.1 Background and Motivation for Mass Spectrometry

Mass Spectrometry (MS) is an umbrella term used to categorize different experimental techniques to detect and measure the mass of particles within a sample. Traditional mass spectrometry techniques typically rely on the charge-to-mass ratio of the particles to differentiate the mass of the sample[1]. MS comes in a variety of forms but some common examples of MS techniques include sector-type detectors, time-of-flight measurements, and ion trapping. Sector-type detectors utilize a magnetic field to deflect ionized particles and direct them toward a detector. The location the particle lands on the detector corresponds to its charge and mass. Time-of flight detectors likewise differentiate particles based on their charge-to-mass ratio by accelerating particles through an electric field and therefore depending on the velocity of the particle, one can determine the mass. Finally, ion trapping is a technique where ions are trapped within an electrostatic field and are either ejected selectively to be measured, or the image current produced by the trapped ions is measured to determine the mass[1, 2].

MS techniques are used in a variety of fields, such as chemistry, biology, and experimental physics. One of the most common uses of MS is for identification of chemical compounds and biologicals, especially proteins[2]. In particular, due to the nature of the measurement, most MS systems require the particle under study (the analyte) to be ionized, which can be accomplished in several ways. For the purposes of this work, we are interested in soft ionization techniques that will result in less fragmentation among the ionized species. Some of the common soft ionization

techniques include electrospray ionization (ESI) and matrix-assisted laser desorption/ionization (MALDI)[10, 11].

Because of the ionization requirement for traditional mass spectrometry, limitations to the effectiveness of traditional mass spectrometry arise from fragmentation of the sample particle. As the analyte is ionized, depending on the procedure, the particle could fragment into its different subunits. This is especially critical for chemical and biological compounds as mass measurements sometimes demands a holistic measurement as opposed to inferring the mass from fragments. For example an organic chemical compound could potentially contain numerous side chains and structures. Ionization could cause these constituents to fragment as they are injected into the mass spectrometry system, resulting in the measurement of the fragments instead of the total mass. While the mass can then be inferred from the relative abundance in a mass spectrometry readout, this is less than ideal. Additionally, traditional MS techniques have limited dynamic range due to electrostatic field limitations and how effective particles can be accelerated or differentiated.

1.2 Background of Nanoelectromechanical Systems

Nanoelectromechanical systems (NEMS) are nanoscale devices that exhibit certain properties which make them interesting to study, both in their ability to explore more fundamental regimes of matter and their various applications to technology. NEMS utilize electrical control of various types to induce mechanical motion, such as the vibrational modes of resonator. Some applications of NEMS include atomic force microscopy (AFM), integrated circuits (ICs), and bio-inspired self-assembly devices[7, 9, 25].

The development of NEMS has also opened the door for mass spectrometry applications due to several valuable properties[16]. In particular, NEMS have a high surface area to volume ratio, low power consumption, extremely low mass, and nanometer length scales to probe on the atomic

scale. These properties improve the sensitivity for measurement as well as reducing physical and electrical footprint of the device. In addition, NEMS resonators, which we focus on in this work, typically have high fundamental resonant frequencies and higher quality factors (Q), which make them ideal candidates for sensitive measurements[8].

1.3 NEMS Mass Spectrometry

From the above discussion, it is clear that NEMS resonators are useful for mass sensing and mass spectrometry measurements. Due to the low mass of NEMS resonators, these devices have an advantage when making sensitive mass measurements[10, 11, 24].

To see how a mass measurement would work, we begin with the resonant frequency ω_0 for a mass-spring system.

$$\omega_0 = \sqrt{\frac{k}{m}} \tag{1-1}$$

Where k is the spring constant, and m is the mass of the moving system. If we Taylor expand the equation to first order

$$\omega_0 + \delta\omega_o = \sqrt{\frac{k}{m}}\left(1 - \frac{1}{2}\delta m\right) \tag{1-2}$$

and then taking the difference between Eq. 1-2 and Eq. 1-1 we get a frequency shift $\delta\omega_0$ that is related to a mass change δm.

$$\delta\omega_0 = -\frac{1}{2}\omega_0\frac{\delta m}{m} \tag{1-3}$$

So in general, as the mass of the system increases, that is as particles are deposited onto the resonator, we expect to see corresponding downshifts in the resonant frequency. We also assume that the frequency shifts and mass shifts are small compared to the resonant frequency and total mass. In reality the actual measurement is more complex, which we cover in the following chapters. However the principle of measuring frequency shifts is the same.

Utilizing NEMS resonators for mass spectrometry also provides an alternative for the ionization step in tradition MS. NEMS-MS only requires the deposition of the particle onto the device to make a measurement, so we are able to perform mass spectrometry by avoiding that ionization requirement. This reduces the potential for degradation or structure changes in more sensitive analytes. In addition, being able to measure only the mass eliminates the charge variable and uncertainty associated with measuring the charge-to-mass ratio in traditional mass spectrometry.

Nonetheless NEMS-MS faces several critical challenges that must be addressed. For general NEMS-MS, depositing particles onto a device poses a challenge due to the extremely small surface area of the device. Additionally particles deposited onto such a tiny resonator may affect the mode shape and therefore the measurement. The deposition step also requires either a preexisting soft ionization technique, such as ESI or MALDI, or a novel technique. Furthermore for this work, we first need to develop the mathematical model for NEMS-MS in two spatial dimensions.

Chapter 2

Circular Membrane Mass Spectrometry

2.1 Mode Shapes

For this work, our main focus is with circular membrane NEMS devices. However we model the dynamics of the system using plate theory, since our devices are actually 3-dimensional systems with finite thickness, even though the devices we use are extremely thin compared to the radius (thickness ~ 1/20 of the radius). Therefore when we refer to the "membrane" we are referring to the NEMS device but assuming it has finite thickness. For these devices there are symmetric radial modes as well as asymmetric azimuthal modes that must be solved separately.

From circular plate theory, we can begin with the equation describing the motion for symmetric displacements that includes a forcing term and a damping term[21].

$$\frac{\partial^2 w}{\partial t^2} + D\nabla^4 w = \frac{1}{r}\frac{\partial}{\partial r}\left(\frac{\partial F}{\partial r}\frac{\partial w}{\partial r}\right) - c\frac{\partial w}{\partial t} + p(r,t) \tag{2-1}$$

where w is the displacement, D is a geometric constant involving the Young's modulus E, Poisson's ratio ν, and the height h. The second and third term on the right hand side of the equation correspond to the damping term, with damping coefficient c and forcing term p. For these devices, we also utilize clamped boundary conditions around the edges of the membrane at $r = r_0$, such that

$$w(r_0, \theta, t) = 0,\ \frac{\partial w(r,\theta,t)}{\partial r}\bigg|_{r0} = 0. \tag{2-2}$$

This equation can be solved via separation of variables and is worked out in detail by Sridhar *et al.* The solution is of the form

$$w_0 = \sum_{n=1}^{\infty} \phi_n(r)[A_n(T_1, T_2, \dots)\exp(i\omega_n T_0) + cc] \tag{2-3}$$

From this, the mode shapes for the symmetric modes have the form

$$\phi_n(r) = a_n[J_0(k_n r) + \mu_n I_0(k_n r)] \tag{2-4}$$

where J_0 is the Bessel function of the first kind and I_0 is the modified Bessel function of the first kind[21]. This is the primary equation we are interested in understanding. The constants are given by

$$\mu_n = -\frac{J_0(k_n)}{I_0(k_n)} \tag{2-5}$$

and a_n, the normalization constant, is defined such that the maximum value of ϕ_n is 1.

$$Max(\phi_n) = 1 \tag{2-6}$$

Furthermore, k_n is found from the roots of the expression

$$I_0(k_n)J_0'(k_n) - I_0'(k_n)J_0(k_n) \tag{2-7}$$

Figure 2.1 shows the graph of the expression used to find the k_n for the symmetric mode. The values for k_n are found in Table 2.1.

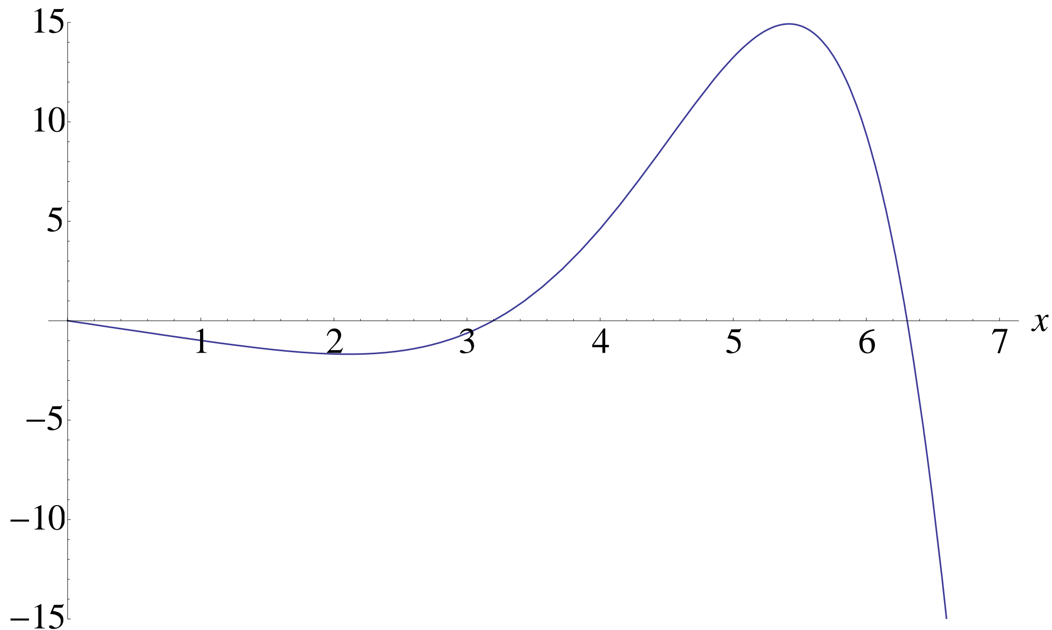

Figure 2.1: Plot of the expression $I_0(k_n)J_0'(k_n) - I_0'(k_n)J_0(k_n)$ showing the first two roots for the symmetric modes, 01 and 02. The first two roots are 3.19622 and 6.30644.

Likewise the asymmetric case can be solved in a similar manner[22]. The mode shapes for the asymmetric case have the form

$$\phi_{nm}(r) = a_{nm}[J_{nm}(k_{nm}r) + \mu_{nm}I_{nm}(k_{nm}r)] \tag{2-8}$$

Like the symmetric case, a_{nm} is the normalization constant and μ_{nm} is defined in parallel fashion. k_{nm} are given by the roots of

$$I_n(k_{nm})J'_n(k_{nm}) - I'_n(k_{nm})J_n(k_{nm}) \tag{2-9}$$

A plot of this expression where $n = 1$ is shown in Figure 2.2.

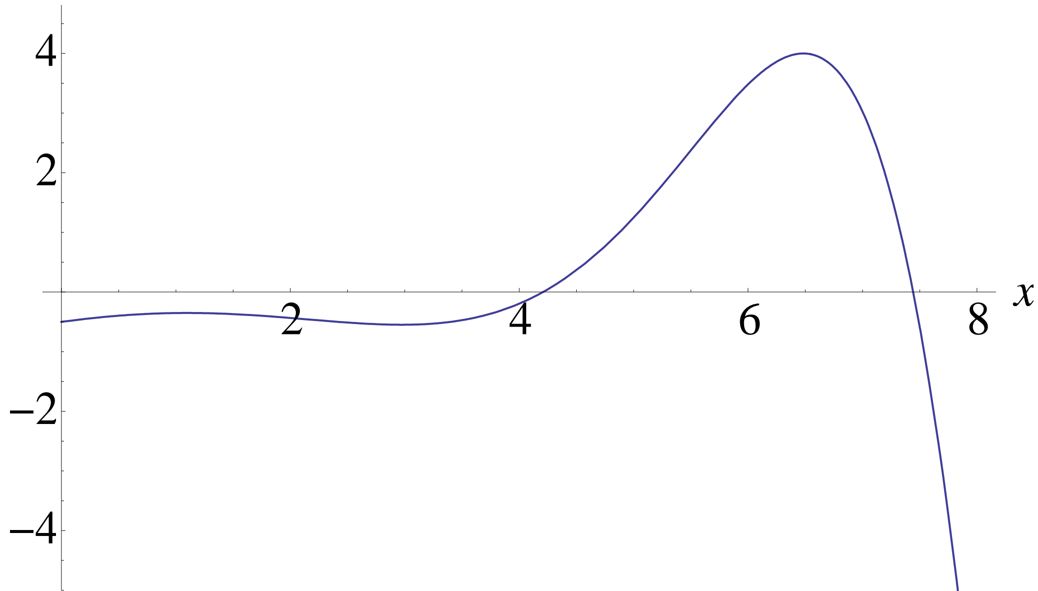

Figure 2.2: Plot of the expression $I_n(k_{nm})J'_n(k_{nm}) - I'_n(k_{nm})J_n(k_{nm})$ for the asymmetric modes, showing the first two roots corresponding to the 11 azimuthal modes and the 21 azimuthal modes. The first root is 4.61090.

For the first asymmetric mode, there will be two degenerate modes, which we call 11_x and 11_y. If the circular plate is completely symmetric radially, then these two modes will have the exact same frequency. This concept will be explored in further detail in Chapter 3.

From this, we can calculate the remaining parameters for the mode shapes. Table 2.1 shows the values for the three constants for the first four modes. Figure 2.3 shows the mode shape as a

function of radius, with the maximum normalized to one. We also model the mode shapes using finite element simulation.

Mode (m,n)	a_{mn}	μ_{mn}	k_{mn}
01 Radial	0.94723	0.05571	3.19622
11_x Azimuthal	1.65780	0.01522	4.61090
11_y Azimuthal	1.65780	0.01522	4.61090
02 Radial	1.00253	-0.00253	6.30644

Table 2.1: Parameters a_{mn}, μ_{mn}, and k_{mn} for the first 4 modes. Note that 11_x and 11_y are degenerate modes and have the same parameters.

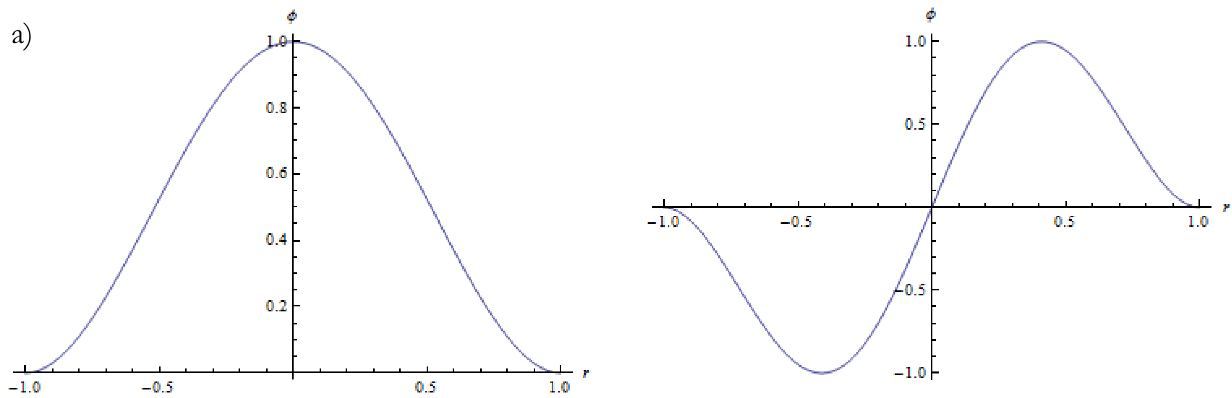

c)

Figure 2.3: a) Plot of the 01 mode shape. b) Plot of 11 mode shape. c) Plot of 02 mode shape. d-g) Finite element simulations of the 01 mode, the two 11 degenerate modes, and the 02 mode.

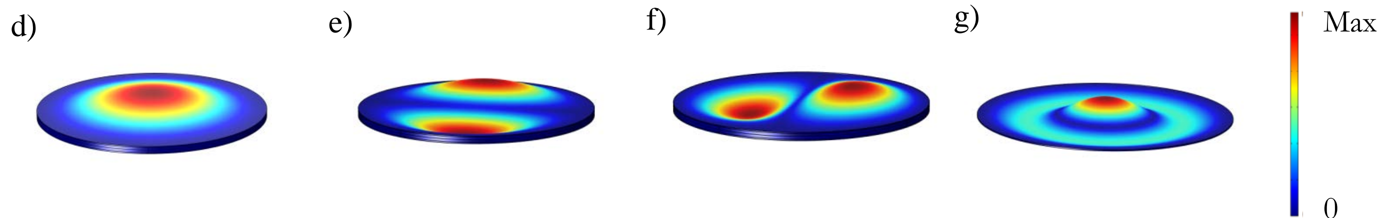

The 01 radial mode is simply the up down mode with the antinode at the center of the device. The 11 degenerate modes have their nodal lines perpendicular to each other and passing through the center of the device. Finally the 02 radial mode consists of two radial antinodes, one at the center and one as a circular ring. We are also interested in the frequencies corresponding to these modes. This will also be explained further in chapter 3.

2.2 Multimode Theory

In Chapter 1, we saw that the resonant frequency of the NEMS device will downshift as mass is deposited onto the device. However we must also consider what is known as the *effective mass* of the system, instead of the total mass, as in Eq. 1-3. The effective mass is a fraction of the total mass and is used to account for the actual amplitude motion of the membrane. Utilizing total mass assumes that every portion of the membrane is moving to the maximum amplitude, like a mass on a spring system, however this is not the case in general for these resonators. To calculate the effective mass we begin with the total geometric mass

$$m_{geo} = \rho \iiint r\mathrm{d}r\mathrm{d}\theta\mathrm{d}z = \pi r_0^2 \rho h \quad (2\text{-}10)$$

But now for the effective mass, we also need to integrate over the normalized mode shape.

$$m_{eff} = 2\pi\rho h \int_0^{r_0} \phi_n^2 r\mathrm{d}r = \frac{2m_{geo}}{r_0^2}\int_0^{r_0} \phi_n^2 r\mathrm{d}r \quad (2\text{-}11)$$

The above equation only holds for the radial modes geometries, but can be generalized for any geometry. We see that the effective mass is affected by the mode shape. Therefore the correction factor for the effective mass is also dependent on the given resonant mode, as defined in the previous section. Table 2.2 shows the values for the effective mass corrections for the first four modes.

Mode	Fractional Correction for Effective Mass
01 Radial	0.18283
11_x Azimuthal	0.36918
11_y Azimuthal	0.36918
02 Radial	0.10189

Table 2.2: Effective mass corrections for the 01, 11, 02 modes.

Replacing the mass from Eq. 1-3 with the effective mass, we have

$$\delta\omega_0 = -\frac{1}{2}\omega_0 \frac{\delta m_{eff}}{m_{eff}} \quad (2\text{-}12)$$

We also wish to represent the change in the effective mass in terms of the mass of the particle. Depending where the particle lands on the device, its effective mass will similarly be scaled by the mode shaped squared at that particular location

$$\delta m_{eff} = \Delta m_{particle}\phi_0^2(r_p, \theta_p) \quad (2\text{-}13)$$

Therefore we have, generalizing to any mode, n

$$\delta\omega_n = -\frac{1}{2}\omega_n \frac{\Delta m_{particle}}{m_{eff}}\phi_n^2(r, \theta) \quad (2\text{-}14)$$

This shows that the frequency shift is dependent not only on the mass of the deposited particle, but also on the amplitude of the particular mode where the particle landed[10, 11]. The above equation is general for all geometries. For the specific case of circular membrane geometry, since the mode shape has positional dependence in two dimensions, (r, θ) or (x, y), we therefore have three unknowns. This is the basis for multimode measurements; in order to decouple the particle mass from its position, we require the measurement of three distinct, yet corresponding frequency shifts. This in itself provides a series of experimental challenges that we will cover in the next few chapters.

Due to the nature of mode shapes as combinations of Bessel functions, the solution can only be found numerically and not analytically. The procedure for solving this system for the 01 and 11 modes is detailed below.

From Section 2.1, we add the two degenerate azimuthal modes in quadrature to eliminate the angular dependence.

$$\phi_{11x}^2 + \phi_{11y}^2 = a_{11}^2\big(J_1(k_{11}r) + \mu_{11}I_1(k_{11}r)\big)^2 \sin^2\theta + a_{11}^2\big(J_1(k_{11}r) + \mu_{11}I_1(k_{11}r)\big)^2 \cos^2\theta$$

$$= a_{11}^2\big(J_1(k_{11}r) + \mu_{11}I_1(k_{11}r)\big)^2 \quad (2\text{-}15)$$

From this, we can numerically solve for the radius by combining with Eq. 2-14 with Eq. 2-15. We divide out the 2π from ω, the angular frequency, to get f, the resonant frequency.

$$\frac{\frac{\Delta f_{11x}}{f_{11x}}+\frac{\Delta f_{11y}}{f_{11y}}}{\frac{\Delta f_{01}}{f_{01}}} = \frac{\phi_{11x}^2+\phi_{11y}^2}{\phi_{01}^2} \quad (2\text{-}16)$$

We then insert the radius back into Eq 2-14 and numerically solve for the particle mass.

$$\Delta m_{particle} = -2\frac{\Delta f_{01}}{f_{01}}\frac{m_{eff}}{\phi_{01}^2} \quad (2\text{-}17)$$

As we can see, this method can only be performed numerically. Below we show modeling results to confirm that this mathematical model is correct.

We first generate random positions on the disk with corresponding particles with random masses. The range of particles is from $40\ nm$ gold nanoparticle (GNP) to $100\ nm$ GNP. The dimensions for GNP refer to the diameter of these spherical particles. We then compute the expected frequency shifts for the first three modes for the random particle at the randomized position with Eq. 2-14. We take these frequencies shifts and following the above method, calculate the radial position to back out the calculated mass. We compare these calculated and generated mass and radii in Figure 2.4.

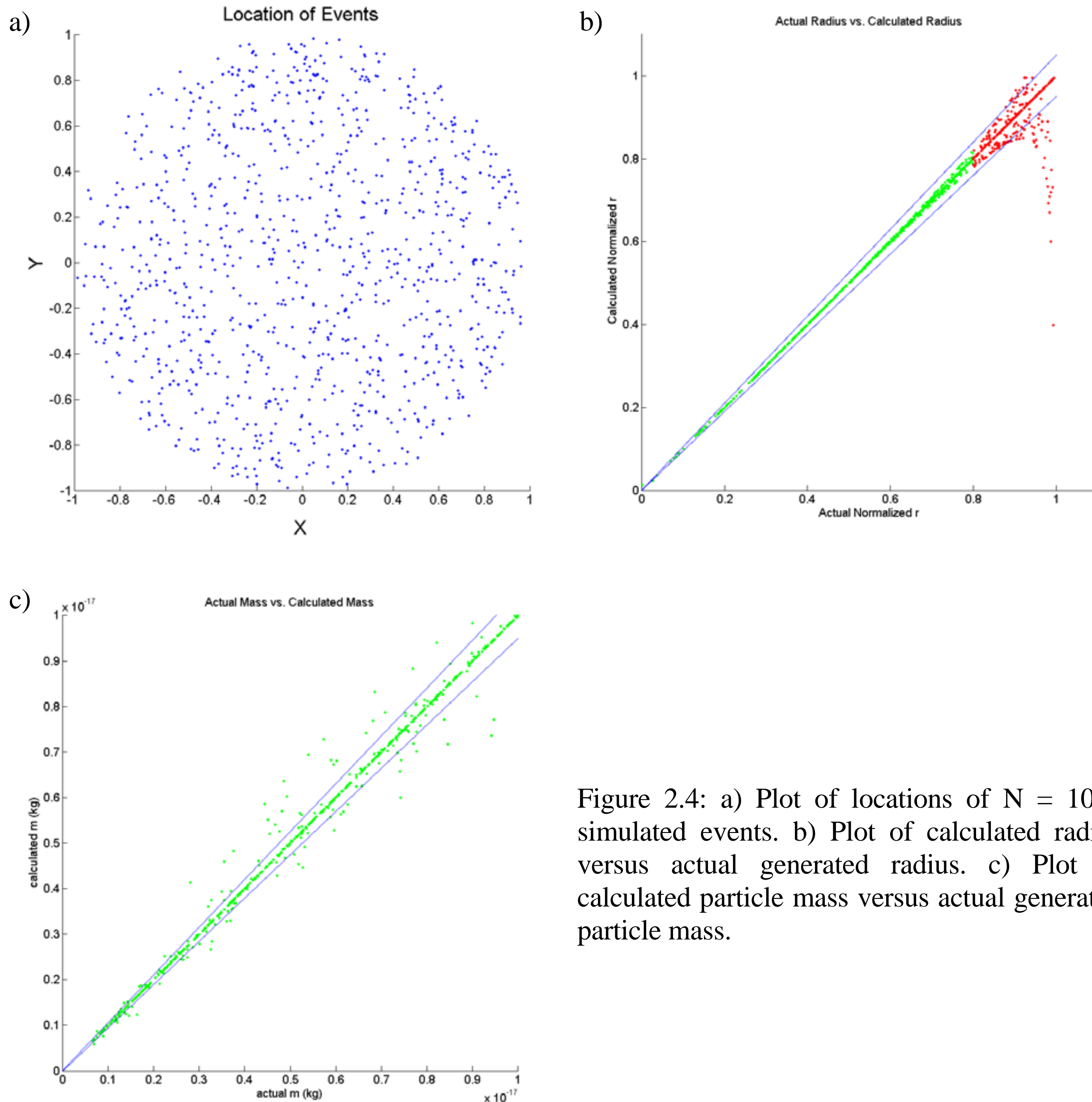

Figure 2.4: a) Plot of locations of N = 1000 simulated events. b) Plot of calculated radius versus actual generated radius. c) Plot of calculated particle mass versus actual generated particle mass.

For the generated locations, we see that we have all events within a circular device of normalized radius 1, as expected. In Figure 2.4b, we plotted the calculated radius for each particle versus its actual corresponding generated radius. We also differentiate for particles at $r > 0.8$, as the calculation become less accurate. The blue lines indicate the 5% accuracy region from the actual radius. In Figure 2.4c, we plot the calculated mass versus the actual mass for only particles at a

radius less than 0.8. Statistically, we obtain about 75% of these particles to remain within 5% of the actual mass.

2.3 Allan Deviation

Another important consideration when performing NEMS MS is the potential mass resolution of the system. In order to characterize the dynamic mass range, we must consider a quantity known as the *Allan deviation*. The Allan deviation, $\sigma_A(\tau)$, is a measure of the frequency stability of clocked systems and can be used to estimate the signal stability that arises from noise processes and drift. The Allan deviation is useful because it can be calculated for a range of integration times, τ, so that we can calculate the optimal measurement time to minimize the noise in a data sample[10, 11].

The Allan deviation is simply defined as the square root of the Allan variance, $\sigma_A(\tau)^2$.

$$\sigma_A(\tau) = \sqrt{\sigma_A(\tau)^2} \tag{2-18}$$

The Allan variance is calculated by taking the difference of two fractional frequency changes. If we have N total data points with a sampling time of τ_{sample}, we can bin the data into M subunits corresponding to some time interval $\tau = a\tau_{sample}$, where a is some integer corresponding to $a = \frac{N}{M}$. The Allan variance is then defined as

$$\sigma_A(\tau)^2 = \frac{1}{2(M-1)} \sum_{m=1}^{M} (y[m+1] - y[m])^2 \tag{2-19}$$

Where $y[m]$ is the average value of the mth bin. We see that the Allan variance is found by taking the difference from adjacent data points rather than from the overall mean. This way we can account for drifts over different time scales and long term drifts will not significantly affect the variance in short time spans.

To measure and calculate the Allan deviation, we need to track the frequency of the system over a long period of time to obtain sufficient data to measure both long term drifts and improve

the statistics. The exact experimental setup will be covered in Chapter 5, however suffice it to understand now that the measurement simply involves frequency tracking over a period of time.

Since we will be utilizing a multimode measurement, it also becomes important to understand the Allan deviation among all three modes. We measured the Allan deviation for all three modes while actuating each mode independently. We also actuate all three modes concurrently to determine if there are any correlation effects between the modes that would affect that measurement. Figure 2.5 shows the Allan deviation for both individual and concurrent actuation.

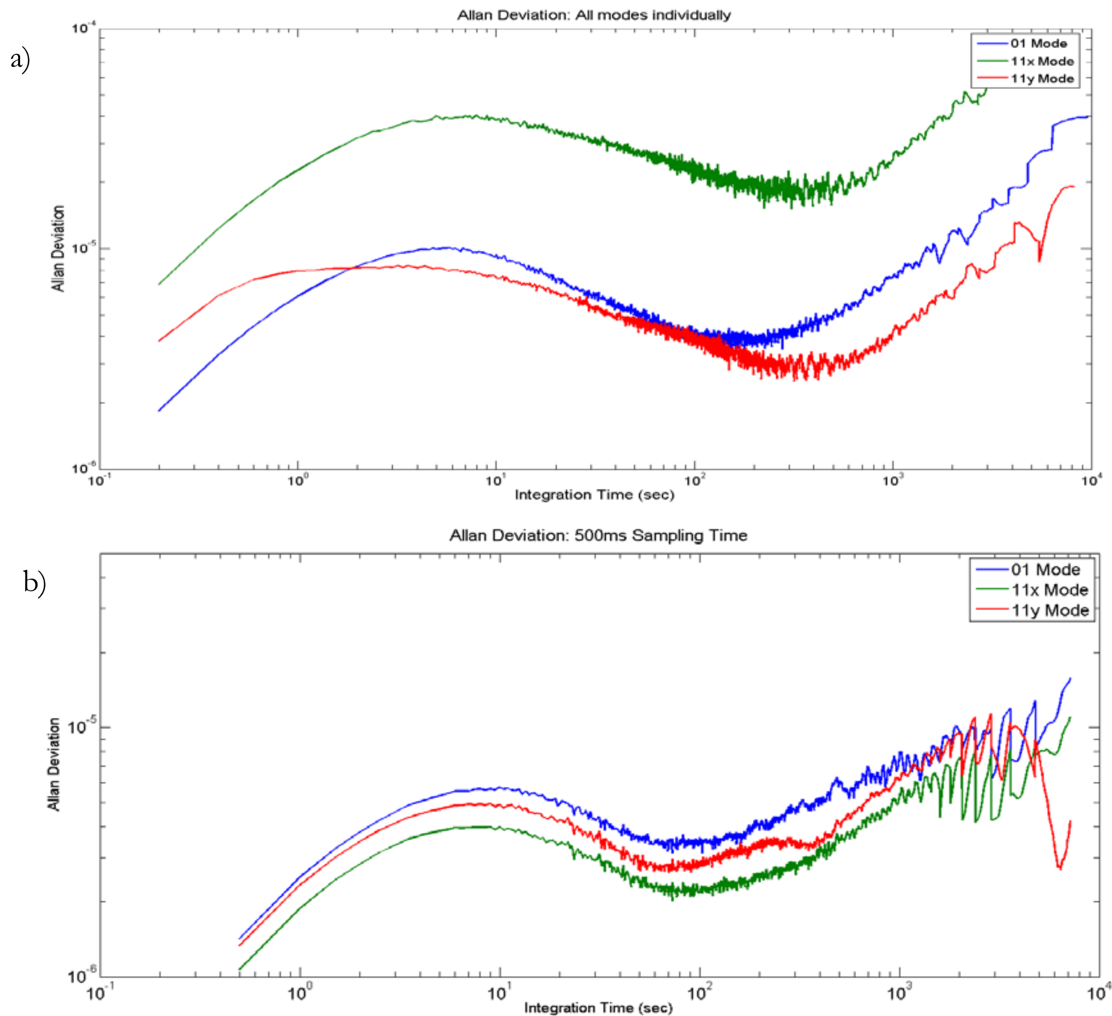

Figure 2.5: a) Plot of Allan deviation when each mode is actuated independently. b) Plot of Allan deviation when each mode is actuated concurrently.

For each measurement, we sample the resonant frequency every $500\ ms$. The data is then parsed into different time intervals and the Allan deviation calculated for each integration time. The upward slopping portion of the graph corresponding to short timescales corresponds to random frequency noise, most likely due to thermomechanical noise and other noise processes. The downward sloping portion is then dominated by the white noise regime and as we average longer, the signal-to-noise begins to improve. The final turn and upward portion is due to long term drift. After a certain time, long term drift begins to set in. The data then become noisy since we have fewer points at longer integration times.

We see that the Allan deviation is not significantly affected by concurrent actuation of the various modes. Since the mass sensitivity is proportional to the Allan deviation (described in the next section), having consistent Allan deviation will help in maintaining consistent measurements.

2.4 Dynamic Mass Range

As we develop this model for NEMS-MS, it is important to estimate the potential dynamic mass range to determine the effectiveness of the system. For the upper bound, we take the measureable mass to be about 1/10 of the device's effective mass. This arises from assuming that the deposited particle is small compared to the overall device mass and can be treated as a point particle relative to the device so that it does not significantly affect the mode shape. Additionally we make this assumption since we only take up to the 1st order term of the Taylor series. Taking higher order would allow us to relax his assumption slightly.

For the lower bound, we begin by approximating the frequency shift by the Allan deviation, since the Allan deviation is a measure of the frequency stability.

$$\frac{\Delta f}{f_0} \approx \sigma_A(\tau) \tag{2-20}$$

Furthermore assuming the particle lands at the antinode of the mode, we get

$$\Delta m_{particle} \approx 2m_{eff}\sigma_A(\tau) \tag{2-21}$$

Therefore we see that the lower bound for the dynamic range is dependent on two factors, the effective mass of the device and the frequency stability of the system.

For these particular devices, the calculated geometric mass is about $18.3\ TDa$ or about $3.03 \times 10^{-14}\ kg$. This gives an effective mass for the first mode, based on the correction from Table 2.2, of $3.35\ TDa$ or about $5.57 \times 10^{-15}\ kg$.

We also need to consider the frequency stability of the system. This is dictated by the noise of the system and can arise from various sources including thermomechanical noise, electronic noise, and photodetector noise. From above, we see that the minimal Allan deviation we can achieve is $\sigma_A(\tau) \approx 10^{-6}$. Inserting this into Eq 2-21 we get a lower bound of the dynamic mass range.

The total dynamic mass range is

$$6.7\ MDa < \Delta m_{particle} < 180\ GDa \tag{2-22}$$

This gives us about a five order of magnitude range for the measureable mass.

Chapter 3:

AlN Device Structure and Operation

3.1 AlN (Aluminum Nitride) Properties

As electromechanical devices attain smaller and smaller dimensions, it becomes important to utilize materials with advantageous electronic properties. The development of more advanced fabrication techniques has also opened the door for testing a wider variety of materials to characterize and select the optimum device material. In particular, piezoelectric actuation for AlN NEMS resonators seems to be a better choice[13]. The details and advantages of piezoelectricity for AlN devices will be covered further in section 3.4.

AlN was first synthesized in the late 1800s, but its potential for electronic application was not realized until the 1900s[18]. AlN is a semiconducting material that when processed into a thin film, exhibits piezoelectric properties that make it advantageous for NEMS devices[6, 23]. Previous work has shown that AlN devices have higher piezoelectric coupling efficiency compared to other piezoelectric devices, such as gallium arsenide. AlN also has a high acoustic velocity and low dielectric loss, which makes it a more suitable candidate for resonators[13].

3.2 AlN Membrane Device Structure

For this particular experiment, we utilize AlN circular membranes. The devices consist of a stack of alternating AlN and molybdenum (Mo). On top of the bulk silicon (Si) and silicon dioxide (SiO_2) substrate is a $50\,nm$ AlN layer (seed layer), a $40\,nm$ Mo layer, a $50\,nm$ AlN layer, and finally a $40\,nm$ top Mo layer. This gives a total device thickness of $180\,nm$. We have also experimented with different thicknesses of devices. The purpose of the stack is to be able to apply a voltage difference across the two Mo layers in order to piezoelectrically actuate the device.

The overall potential effective region of the device is about 8 μm in diameter based on the gold contacts patterned onto the surface, however the exact device dimension is unknown since the released region is hidden below the surface. The top Mo layer also contains several important fabrication features. The cuts across the top Mo layer dividing the surface into four quadrants and exposing the top AlN layer acts as an aid to help induce the actuation of the degenerate modes. A bridge cut is also made on one of the top Mo quadrants to further isolate the motion of that quadrant to null out the background in certain measurement schemes. A hole is also created in the center of the device and tunnels all the way through the piezoelectric layers to the base SiO_2 layer. This allows us to release the device via a wet etch, as hydrofluoric acid (HF) can etch away the silicon dioxide layer.

The schematic in Figure 3.1a shows what the released underside of the device should appear like, assuming a perfectly isotropic etch. From the scanning electron microscope (SEM) images in Figure 3.1, we see both an overview of a set of devices (six total per pattern) and a magnified image of one device. In the overview, the large polygon-shaped regions are the six gold contacts for each device. The two horizontal contacts on either side are grounds connected to the bottom Mo layer and the four other contacts correspond to the contacts on the four quadrants of the device on the top Mo layer. In the zoomed in image, the darker area corresponds to the top Mo layer and the lighter cut portions are the exposed top AlN layer. The medium gray shade is the edge of gold contacts.

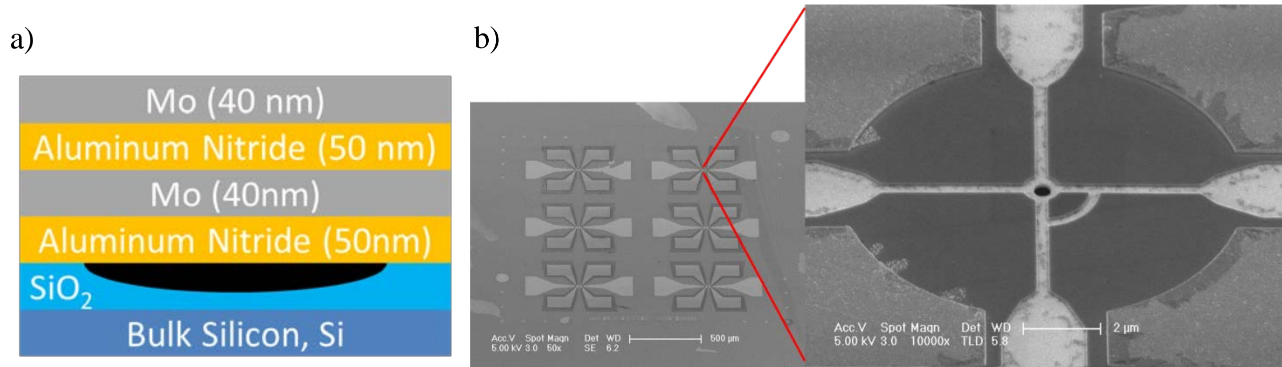

Figure 3.1: a) Schematic and dimensions of the piezoelectric stack. (Image not to scale) b) SEM images of the array of devices and magnified image of a single device.

The exact first mode frequency for a circular plate is given by the equation

$$\omega^2 = \frac{40.704^2 E h^2}{12\rho(1-\nu^2)d^4} \tag{3-1}$$

where E is the Young's modulus, h is the height of the plate, ρ is the density, ν is the Poisson's ratio, and d is the diameter. From this, if we assume a diameter of about 6 μm, we get a frequency around 70 MHz which lines up with the measurements we describe in Chapter 4.

3.3 Overview of Fabrication Procedure

The fabrication of these devices is a multistep process following standard nanofabrication procedures. We begin with prepared Si wafers containing the AlN stack. We then follow six step of electron beam lithography. The first step is to write a mesa layer to etch away the top Mo and top AlN layer from all regions except where the device will be located. We then write alignment markers and evaporate gold onto them to act as guides during the remaining steps. The third write is known as the cut layer and has two components, a high resolution cut and a course cut. The high resolution write is to create the cross to isolate the four quadrants and bridge cut on the top Mo layer of the device. The course cut is to electrically isolate the exposed bottom Mo layer in order to create contacts. We then write the hole which goes all the way down to the oxide layer for HF

etching. Then we write the isolation layer, which is used to evaporate strontium fluoride. This acts as an isolation layer between the gold contacts and the bottom Mo layer, which is typically grounded. Finally we write and evaporate the gold contact layer.

Once we are ready to use the device, we wet etch the device. We expect the HF etch to be isotropic, so we expect a circular released device. We etch for 19 minutes, to obtain a device with radius between 2 and 4 μm. The exact etch rate depends on the quality of the oxide and etch solution.

3.4 Actuation Techniques

In order to measure the frequency of NEMS devices, we need to be able to actuate them to drive the resonant modes. Throughout the NEMS community, there are several ways to actuate the device, including capacitive, magnetomotive, and via piezoshakers. For these AlN devices, as mentioned earlier, we choose to actuate these devices piezoelectrically due to better transduction efficiency[13].

Piezoelectricity is a property of materials that was first discovered in the 1880s. In general, piezoelectricity refers to when a material is deformed mechanically, internally the structure generates some sort of electric charge. This typically arises from when the applied stress causes a change or reorientation of the dipoles in the material, altering the electric field in the material. Conversely, piezoelectric materials, when applied an applied electric field, can react with mechanical strain, deforming the material. In most cases, this piezoelectric property is reversible in both the mechanical/electrical variations as well as the direction of the piezoelectric pathway. The piezoelectric properties of the material are classified by the piezoelectric constants d_{xy} which relate the strain to the polarization. In particular, AlN was found to have higher piezoelectric

coefficients, making it a more effective transducer of an applied electric field to mechanical motion. Therein lies the advantage of utilizing AlN as a piezoelectrically actuated NEMS device.

To piezoelectrically actuate these AlN stack devices, we utilize the setup show in Figure 3.2. We apply an alternating current (AC) signal generated by the network analyzer (NA) to the top Mo layer and ground the bottom Mo layer, creating an electric field in the vertical direction. This induces the strain on the device that causes it to vibrate out of plane (up and down). Depending on the AC frequency, we can drive the devices to resonance. For the multimode measurement for mass spectrometry, we combine multiple driving signals that will actuate each individual mode.

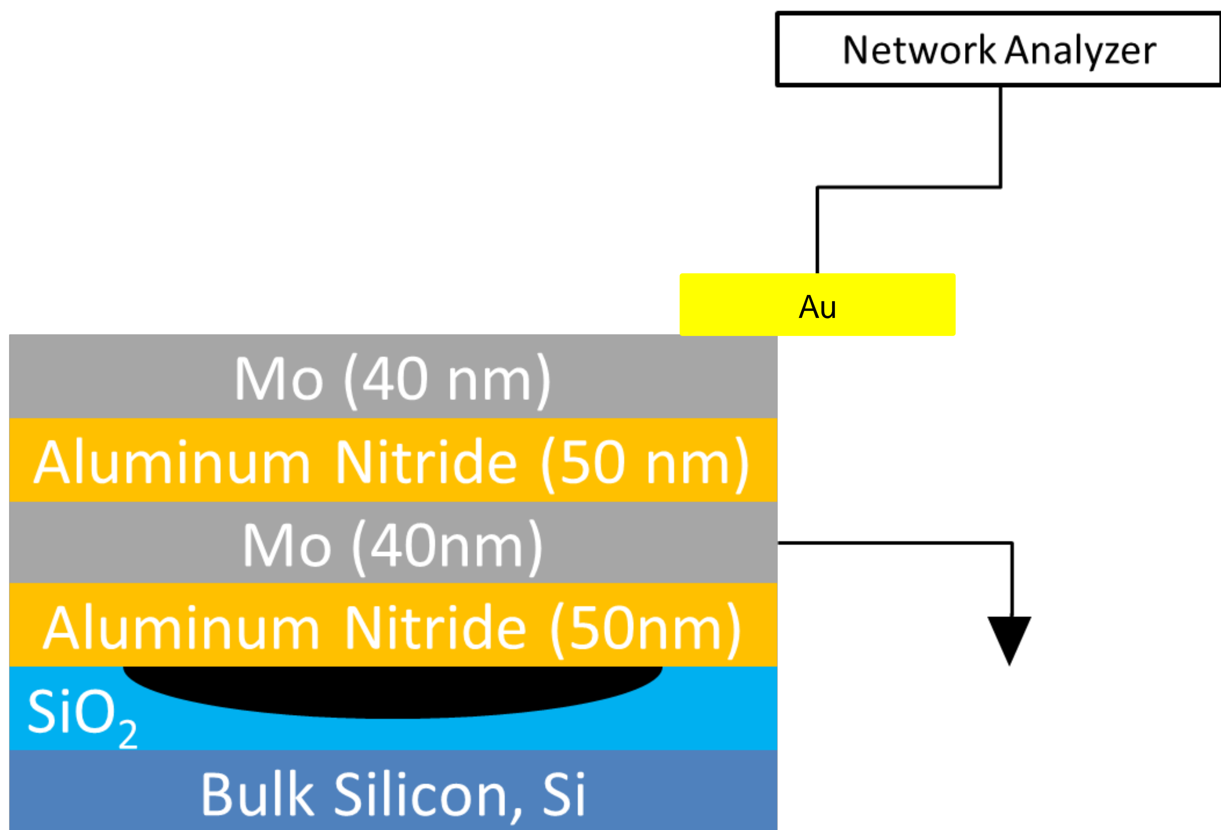

Figure 3.2: Actuation scheme for these piezoelectric devices.

3.5 Detection Schemes

Likewise there are also several techniques to detect and measure the response of NEMS systems, including direct imaging, magnetomotive, and piezoresistive. For this experiment, we study two specific types of detection: optical and electrical. The bulk of the work focuses on optical measurements, with some piezoelectrical detection to confirm the measurements.

Optical detection is the primary detection scheme that we choose to use. The advantages of optical detection include reduced capacitive background that we see in electrical detection as well as the ability to spatially map the response[12, 13, 15]. A detailed schematic of optical detection is show in Figure 4.1. The detection laser is placed at normal incidence to the surface of the membrane device. The beam is directed through a beam splitter and towards the surface of the device. In order to detect the vibration, we utilize interferometry with the path length difference when the light reaches the surface of the device. The laser light is reflected and returned to the beam splitter where it is directed into a photodetector. From this we can then record the amplitude of the response. The disadvantage of optical detection, however, is that it requires alignment of the optics, which can become a laborious task.

A second technique that we explored was a piezoelectric detection technique. This method takes advantage of the piezoelectric properties of the device. As the device is driven, we can measure the electrical response generated through the piezoelectric effect. The disadvantage of this technique is that it produces a significant capacitive background due to charging between the large area of the gold contacts and conducting substrate.

Chapter 4:

AlN Device Characterization and Measurements

4.1 Optical Detection Setup

For the remaining part of this experiment, we exclusively focus on the optical detection technique, unless otherwise noted. A more detailed schematic of the experimental setup is shown in Figure 4.1. We begin with a red, HeNe laser with a wavelength of 633 nm. The laser is directed through a beam collimator, a beam expander, and then a beam splitter. The laser is then focused through a lens and is directed into the sample chamber. The lens is mounted on a ThorLab XYZ motorized stage to control the position of the laser incident on the device with a step size resolution of $0.2\mu m$.

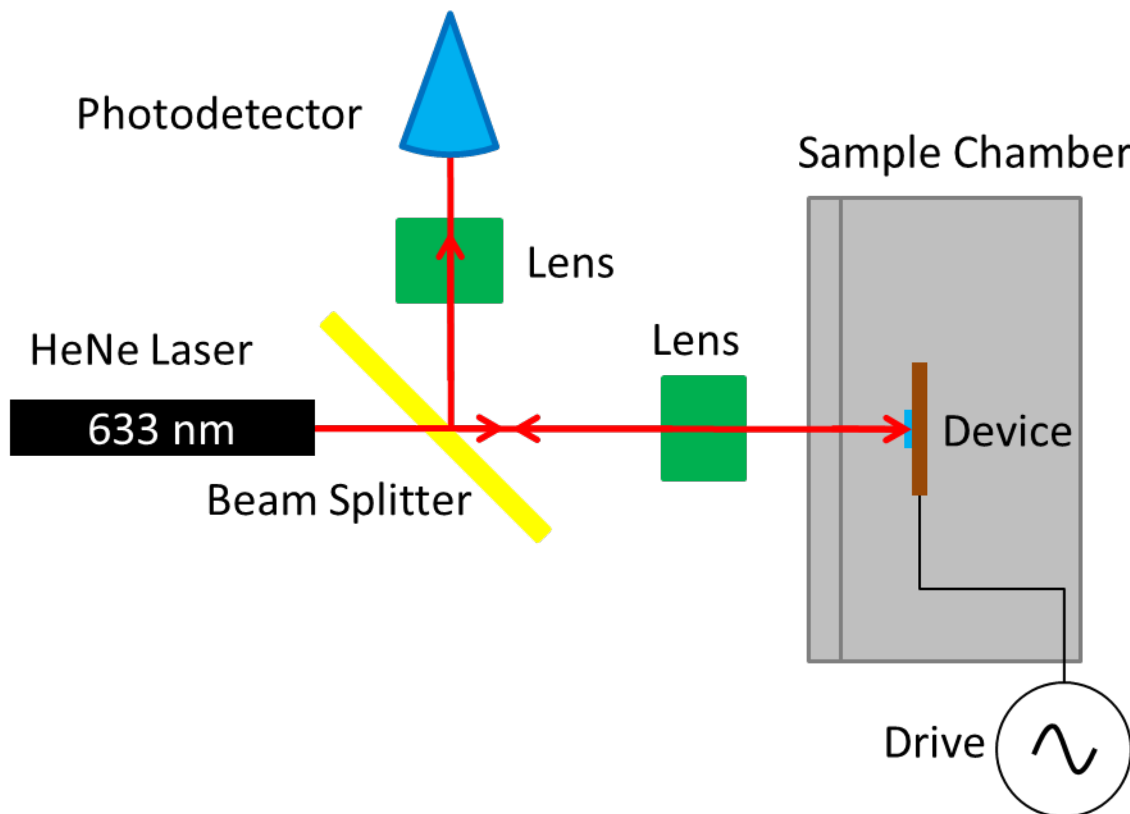

Figure 4.1: Schematic of the optical detections setup.

The sample chamber is an approximately 6” diameter aluminum cylinder with modifications for optical detection, a vacuum connection, and electrical connections. On the front side, a 2” round opening is fitted with a quartz window to allow the optical detection laser to enter. The side of the chamber contains an opening to connect vacuum components to pump down the chamber and the back panel contains eight electrical SMA outputs. Internally, the chamber contains an elevated, adjustable stage to mount the chip carrier. The chip carrier is a ceramic holder that contains gold contacts that pass through the ceramic to electrical readout pins. A typical chip carrier that we use contains 64 possible pins. To connect the device to the chip carrier, we wire bond the contacts on the chip carrier to the contacts on the device. We can then map the device electrodes to the pin readouts. Figure 4.2 shows a more detailed image of the chamber and sample carrier.

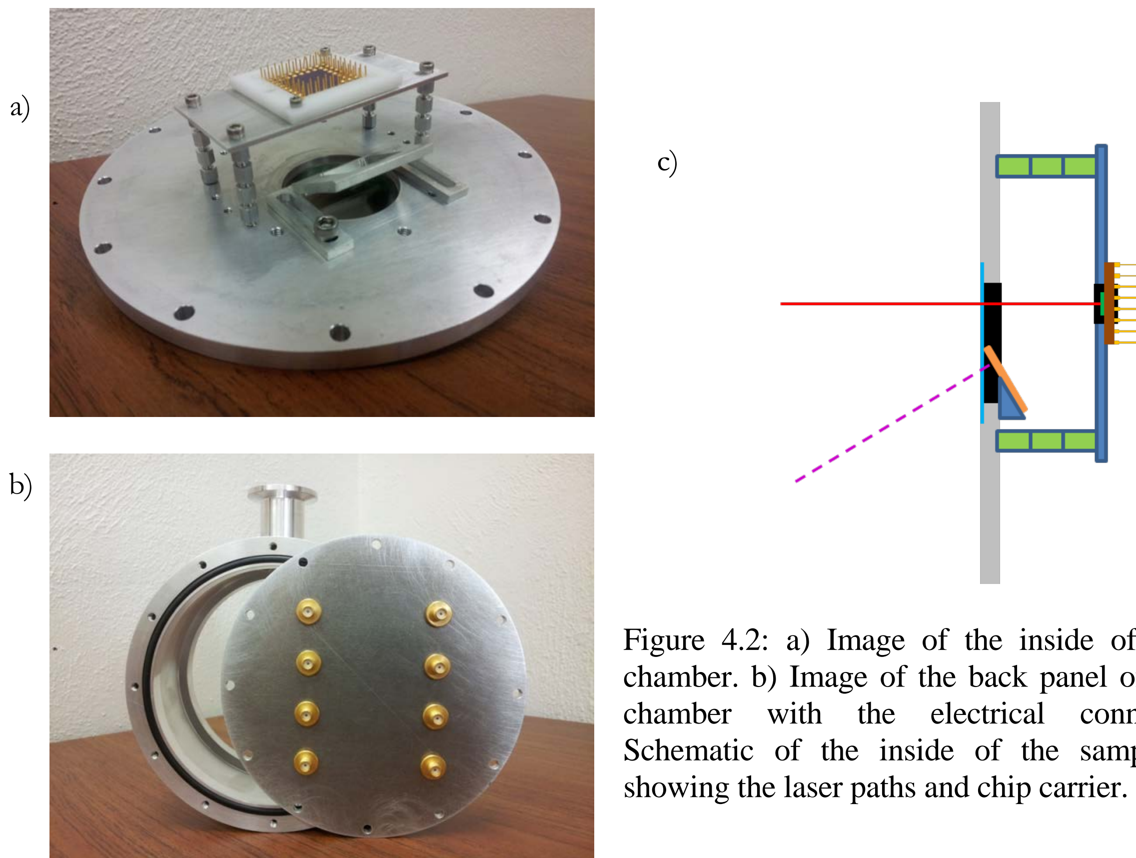

Figure 4.2: a) Image of the inside of the sample chamber. b) Image of the back panel of the sample chamber with the electrical connections. c) Schematic of the inside of the sample chamber showing the laser paths and chip carrier.

After the optical detection laser enters the chamber, it is reflected off the device and returns to the beam splitter and is then directed into the photodetector. The interference pattern arises from the path length difference between either the device surface and the substrate or the device surface and the quartz window. From this, we can readout the responsitivity of the device. The electrical readout of the photodetector is connected to the input channel of a network analyzer.

4.2 Spatial Response Scan

After loading the device into the chamber and pumping down the system to about $10^{-5}\ torr$, we can manually focus the laser onto the device by following the projected image on a piece of paper. Utilizing the NA, we sweep over a wide range of frequencies to identify the resonant peaks. We focus on the lowest frequency peak which we expect to correspond to the 01 radial mode. We manually sweep in the X, Y, and Z direction of the motors to optimize the position of the laser on the device and the amplitude of the signal. We define X, Y to be in the plane of the device and Z to be the focus direction of the lens. We are looking for the very center of the device because we expect the amplitude of the response to be maximal there since that is the location of the antinode of the first mode.

Following our manual rough optimization, we can perform a more systematic 3D XYZ scan of the laser position to finely optimize its position, especially in the focal plane. This is done iteratively by first stepping through each X position for a given Y and Z position, then moving to the next Y position and repeating the step through of the X direction. After completing a set of Y scans, the program takes the next step in the Z direction and repeats the scan of the XY plane. The XYZ motorized stage is controlled through LabView via a Universal Serial Bus (USB) connection. At each position, the NA takes a frequency sweep of the selected frequency span via a General Purpose Interface Bus (GPIB) between the NA and computer. After each sweep, the program picks

out the frequency, amplitude, and phase that corresponds to the maximum amplitude of each sweep and stores that information. When the entire scan is complete, we can plot the max amplitude as a function of laser position. We can also plot the corresponding frequency, the real component, and the imaginary component of the response at the maximum amplitude location. From this, we can spatially map out the device to identify the optimal location for the detection laser.

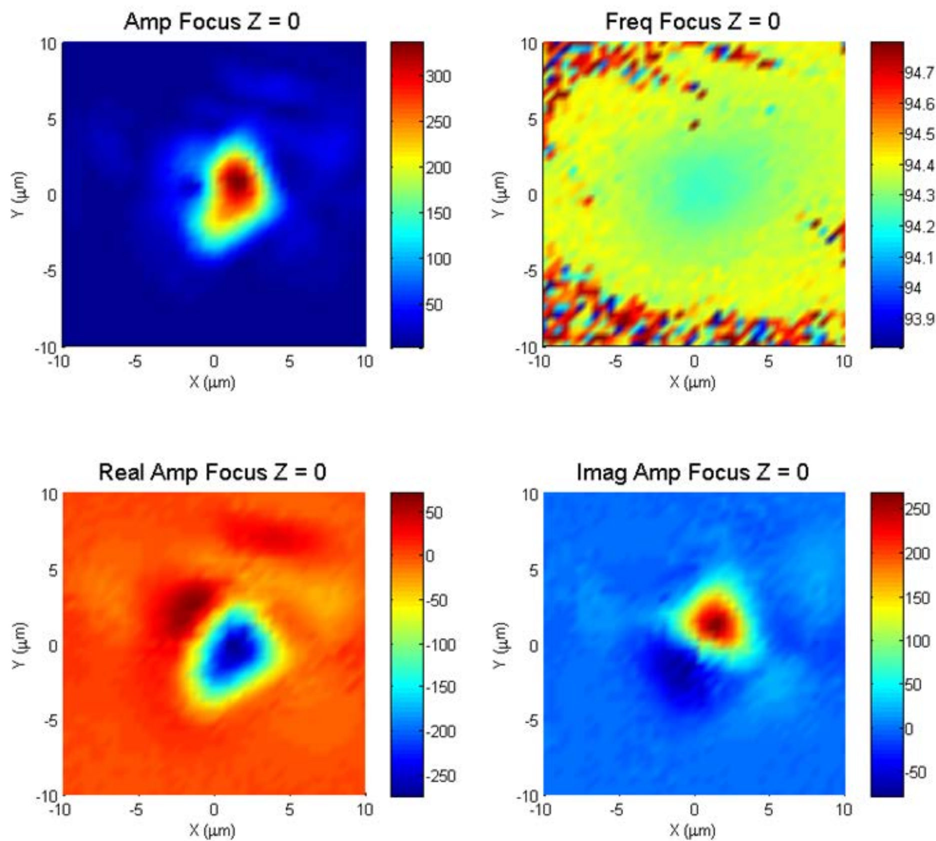

Figure 4.3: Plots of a 3D scan at one focus. The upperleft plot is maximum amplitude at each position. The upperright shows the corresponding frequency to the maximum amplitude and the lower two plots show the real and imaginary components.

This particular scan was taken with a new batch of devices with a 145 nm device layer and thinner top Mo and bottom AlN layers which changes the stiffness of the device. Also the SiO_2 layer etched slower in this device, so the radius was smaller and therefore the frequency was higher. Nonetheless for the first mode, we see that the signal is well localized and that the response dies off further away from the center of the device. Additionally the real and imaginary components of the

signal have the expected shape. For this particular device, we see a fundamental mode at about 94.2 MHz. For the frequency plot in the upper right, we see a central blue patch that corresponds to about 94.2 MHz, however as we move radially away from the center, we see that the frequency increases. This may be due to some heating effects from the laser, where the center of the device is heated and the material is slightly softer, which would lower the true resonant frequency. This difference is about 1% of the total resonant frequency.

Another consideration is the convolution of the laser spot size with the size of the device. The spot size of the laser is about 5μm, so this is comparable to the size of the device. Therefore there is some convolution with the exact readout, which is why the effective device area seems slightly larger than in reality. From finite element simulations of these devices, the corresponding radius for a 94.2 MHz device is about 2.3 μm. Similarly for the first generation of devices that have the thicker 180 nm stack dimensions as described in section 3.2, the frequency of 70 MHz corresponds to a device size of about 2.8 μm.

We perform the same scan for the higher order modes as well, mapping out the device when driven at the 11 azimuthal modes. The plots are shown below in Figure 4.4.

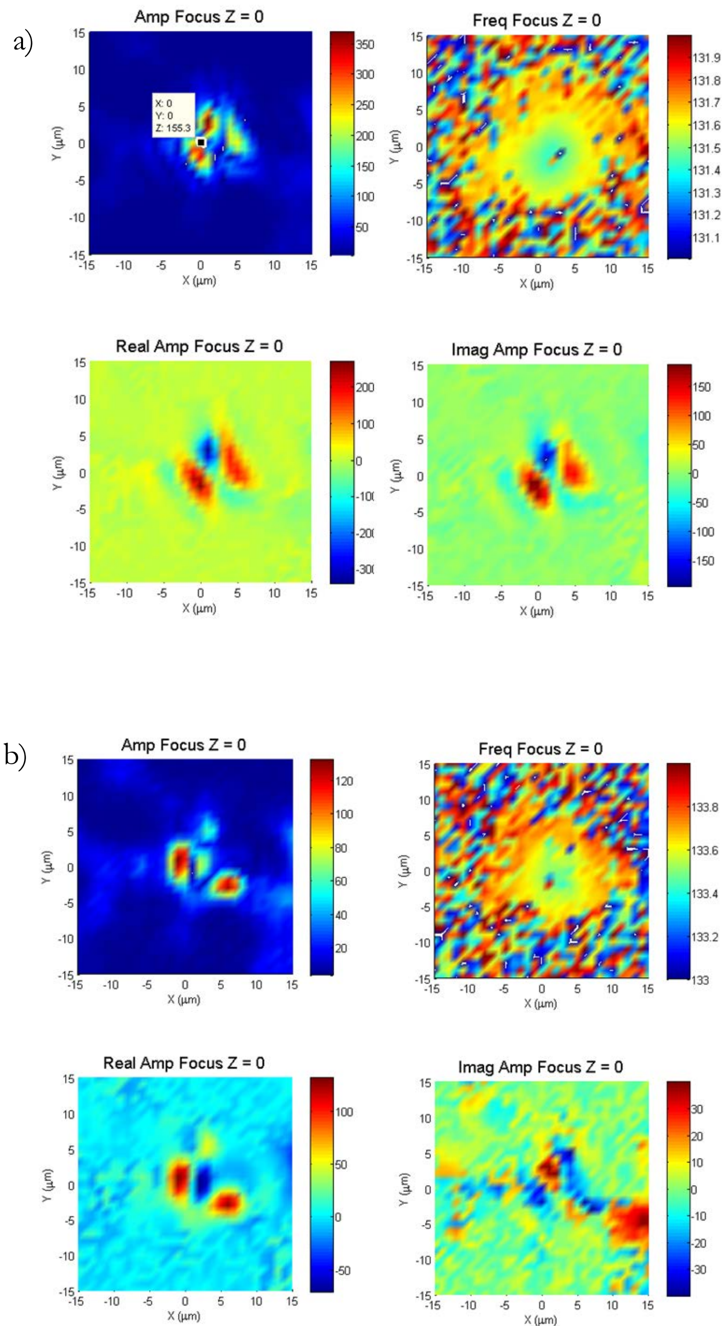

Figure 4.4: a) Plots of a 3D spatial scan for the lower degenerate mode at 131 MHz. b) Same 3D scan at the higher degenerate mode, 133 MHz.

These plots were taken with devices with the original thicker dimensions. Looking carefully at the two amplitude plots for this higher mode, we see the alternating lobes of the azimuthal mode. Additionally the signal is well localized, so this resonance is indeed mechanical. The

corresponding frequencies are about $131\,MHz$ and $133\,MHz$. The cause of this frequency splitting will be detailed in the next section. These frequencies match up well with the predicted frequencies from theory and finite element simulations. Also, there is potential to attempt to release the devices for a longer period of time to increase the radius and lower the frequency. This will be useful to allow measurement of even higher modes. Currently we are limited to a maximum frequency of $200\,MHz$ by the measurements equipment.

Comparing the positions of all three modes, we need to select a laser position that optimizes the response of all three modes. For example, selecting the maximum for the 01 mode theoretically corresponds to the nodal lines for the degenerate modes, so in practice we want to offset the laser position slightly. Furthermore, the transduction efficiency of the higher modes is lower since we require more energy to actuate them. Therefore we choose a location that can provide the greatest response for the higher modes. The 01 mode typically has a much higher signal-to-noise ratio, so we can move off the antinode of the first mode while still maintaining a high signal-to-noise ratio.

4.3 Frequency Sweeps

The next step is to characterize the responsivity of the device because it is important to understand the physics of the device to effectively use it for mass spectrometry. This is done by performing more specific frequency sweeps with the network analyzer by applying different drives to the device and by averaging each sweep for a longer period of time. We expect that as we increase the voltage applied to the device, the amplitude of the response will increase. At a certain point, the response will become nonlinear. Amplitude sweeps of the first mode is shown in Figure 4.5.

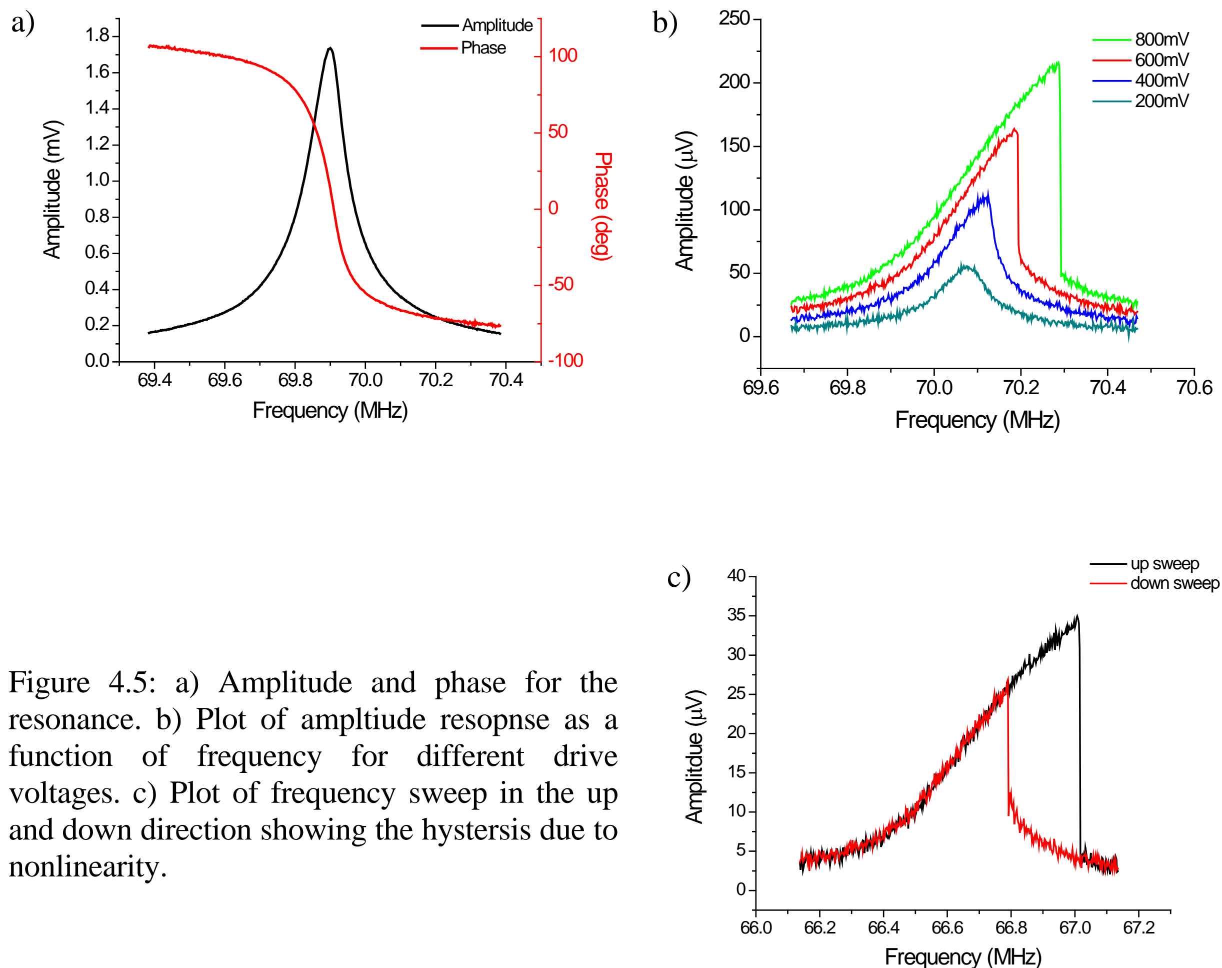

Figure 4.5: a) Amplitude and phase for the resonance. b) Plot of ampltiude resopnse as a function of frequency for different drive voltages. c) Plot of frequency sweep in the up and down direction showing the hysteresis due to nonlinearity.

Each of the above plots was taken from different devices, but from the same batch of devices. The central frequencies are all slightly different due to the uncertainty from the radius of the device during the releasing process of fabrication. Additionally the amplitude response of each device is slightly different due to fabrication variations that can affect the efficiency. This is one major challenge as we attempt to scale up the system to arrays of devices. We have measured first mode resonances with amplitudes as low at 10's of μV to as high as $1\ mV$. The Q factor for the first mode is approximately 650.

As we see from Figure 4.5a the phase goes through an $180°$ phase shift as it passes through the resonance. In Figures 4.5b, we see the nonlinear response of the devices. This is characterized

by the increasing resonant frequency as well as the sudden sharp drop off in amplitude. For resonances in general, nonlinearity can arise from a variety of sources, including fabrication defects, natural damping, and the measurement scheme. For these devices, we believe that the nonlinearity is geometric and arises when we drive the device beyond their linear limits; that is where the amplitude of its motion is far greater than its thickness. This geometric effect leads to a positive Duffing term, which results in a higher resonant frequency[17]. We also see the hysteresis depending on the direction that the frequency is swept, further indicating the nonlinear response. The nonlinearity further confirms that we are looking at a real, mechanical resonance from the device.

We also sweep the frequency of the higher 11 degenerate modes. We see that the supposedly degenerate modes have a frequency splitting of about 1.5 MHz between the two modes. Across the different devices we have measured, we have seen frequency splitting anywhere from being almost perfect degeneracy to 2 MHz. This frequency splitting is caused by asymmetry during the fabrication process that breaks these modes. For example the alignment of the cross cuts in the top Mo layer may not be perfectly symmetric or the HF release was not perfectly isotropic. This characteristic is actually very useful for mass spectrometry because we can utilize these two modes as part of our measurement, rather than looking for higher order modes. For the device scanned in Figure 4.6, we see resonant frequencies for the degenerate modes at about 131 MHz and 132.5 MHz. For these higher modes, we have been able to see amplitudes between 10's of μV up to 100's μV. The overall transduction efficiency of these modes is lower since these modes are much more difficult to actuate compared to the fundamental mode, hence why we include the cuts. For the linear resonances, we get a Q of about 750. Again we see that we can achieve non-linearity when we increase the drive amplitude.

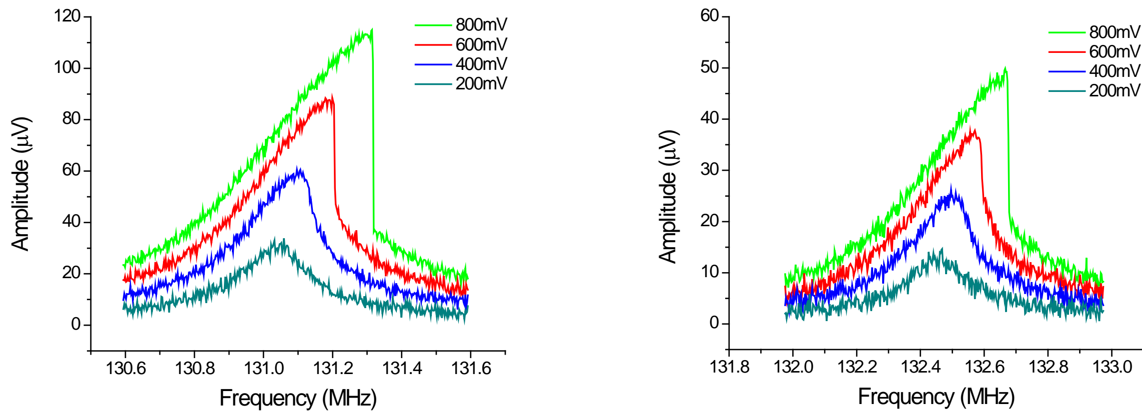

Figure 4.6: Frequency sweeps of the higher 11 degenerate modes with various drives.

4.4 Piezoelectric Detection Measurement

To further test and characterize the device, we also attempted to piezoelectrically measure the response of the device. This is done by reading out the response from an alternate electrode on the membrane and feeding that signal directly back to the NA, versus optically detecting the resonance. As previously mentioned, this measurement arises from the piezoelectric properties of these devices. As we apply a voltage to the device, it generates a voltage that we read out. Figure 4.6 shows what a typical measurement would look like. We see that we have a very large linear background ($> 20\ mV$), which makes identifying the peak more difficult. Nonetheless we do see the expected

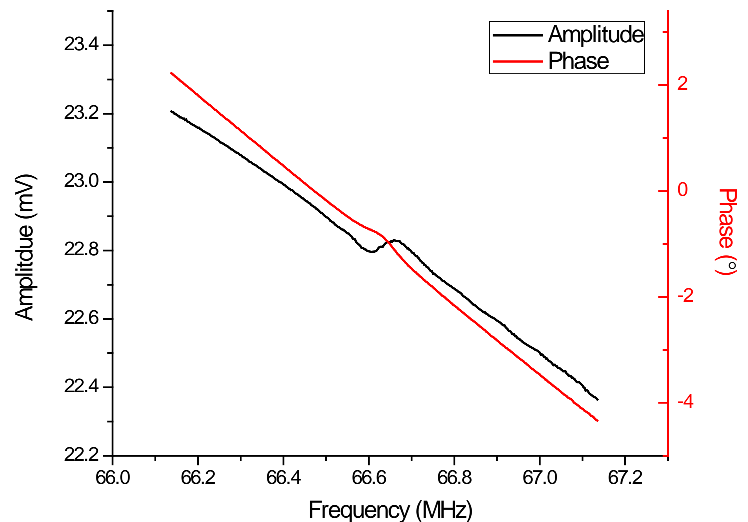

Figure 4.7: Frequency sweep of the fundamental mode of a device at 66 MHz utilizing piezoelectric detection.

resonance peak for the 01 radial mode. To fit this Lorentzian, we set the fitting function within Matlab to remove 95% of the background. We obtain a $Q \sim 800$ for electrical detection.

Ultimately we will choose to utilize optical detection for the mass deposition system because it produces cleaner signals and has the ability to spatially scan the device to visualize the mode shapes.

Chapter 5:

Mass Spectrometry Experimental Setup

5.1 Optical Detection/Mass Deposition Setup

After the devices are characterized, we can attempt to mass load. To do this, we modify the typical detection setup to be able to incorporate the mass deposition portion of the experiment. The first adjustment is to offset the quartz window so that we can accommodate both the detection laser, which will be centered with respect to the aluminum cover, and the UV laser for mass deposition, which will be incident at an angle to the device. Therefore the window itself is not centered with respect to the chamber, but rather offset towards the right based on the orientation of our setup. On the inside surface of the front cover containing the quartz window, we place an angled bracket used to mount mass sample slides. The detailed schematic of the chamber is shown in Figure 4.2. The UV laser is aligned so that it is normal to this sample slide, but positioned such that the deposition process will have flux directed towards the device. The UV laser is a pulsed $355\ nm$ beam that is focused through a second lens that can be controlled with its own XYZ motorized stage. The pulse rate is triggered with a function generator set to a pulse waveform. A schematic and picture of the aggregate setup is shown in Figure 5.1.

The mass deposition technique we use is known as MALDI. Since we are initially testing GNPs, we can utilize this soft ionization technique. MALDI involves an energy transfer when the UV laser is pulsed onto the back of the sample. The matrix that the analyte is embedded in absorbs the UV energy and transfers it to the particle. The energized particle are then desorbed off the sample into the sample chamber and towards the device.

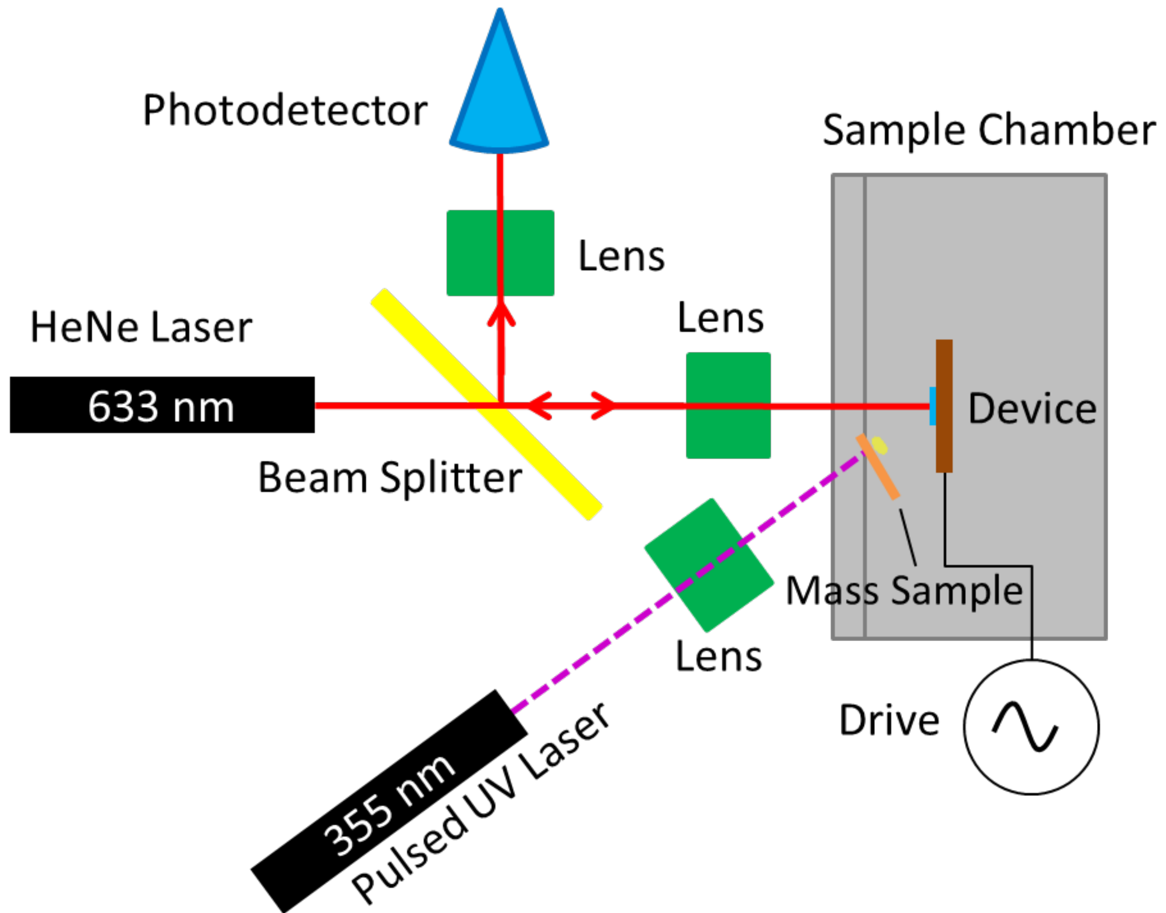

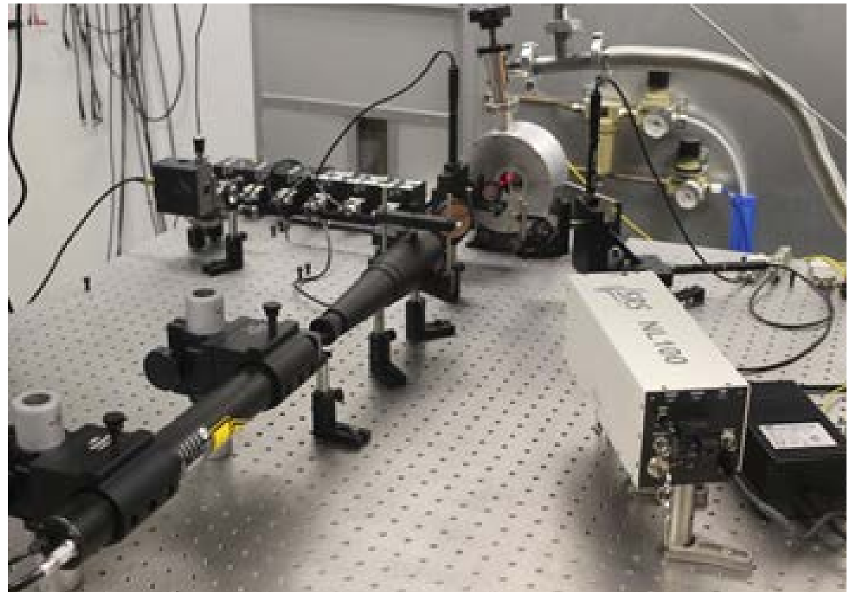

Figure 5.1: a) Schematic of the optical detection plus mass deposition setup. b) Picutre of the experimental setup.

5.2 Phase-locked Loop Setup

In order to track the frequency of all three modes in real time while attempting to mass load the device, we utilize a phase-locked loop (PLL) measurement setup. In general, a PLL is a technique that takes in two signals, a test frequency and a reference frequency, and compares the two phases. Based on the phase difference, a voltage controlled oscillator (VCO) outputs a signal with a phase relative to the phase of the reference. This type of circuit is useful when the frequencies change and the PLL can adjust the frequency by looking at the relative phase of the two systems. Hence we see the usefulness of such a setup to track frequency shifts from mass deposition events[14].

For our PLL experimental setup, we utilize a set of three SRS844 high frequency lock-in amplifiers and three function generators to take measurements. For each mode, we feed a drive signal from the function generator into both the device and the reference input for the lock-in amplifier. For the first mode, we utilize an Agilent 33250a waveform generator since the frequency is below 80 MHz. This particular function generator has a built in reference output so we do not need to split its output. For the two higher modes we utilize HP8648 function generators since they can output higher frequencies, up to several gigahertz. These HP8648 function generators do not contain reference outputs, therefore the output signal is split via a power splitter and fed into the corresponding lock-in amplifier's reference input. For each mode, the input signal from each function generator is combined with the other two modes by using a power splitter as a combiner and then connected to an electrode on the device. The output signal from the photodetector is split into the input of each respective lock-in. The lock-ins and function generator are controlled via GPIB from a LabView program. A diagram of the experimental measurement setup is shown in Figure 5.2. The PLL measurement continuously tracks the frequency and continuously corrects the drive frequency to account for any shifts in resonance, such as from a mass loading event. The

advantage of using this technique, versus continuous frequency sweep with a network analyzer is that we can rapidly record data by only picking out the resonance frequency based on the phase. Additionally this allows faster switching between measuring each mode, rather than waiting for an entire frequency sweep to finish.

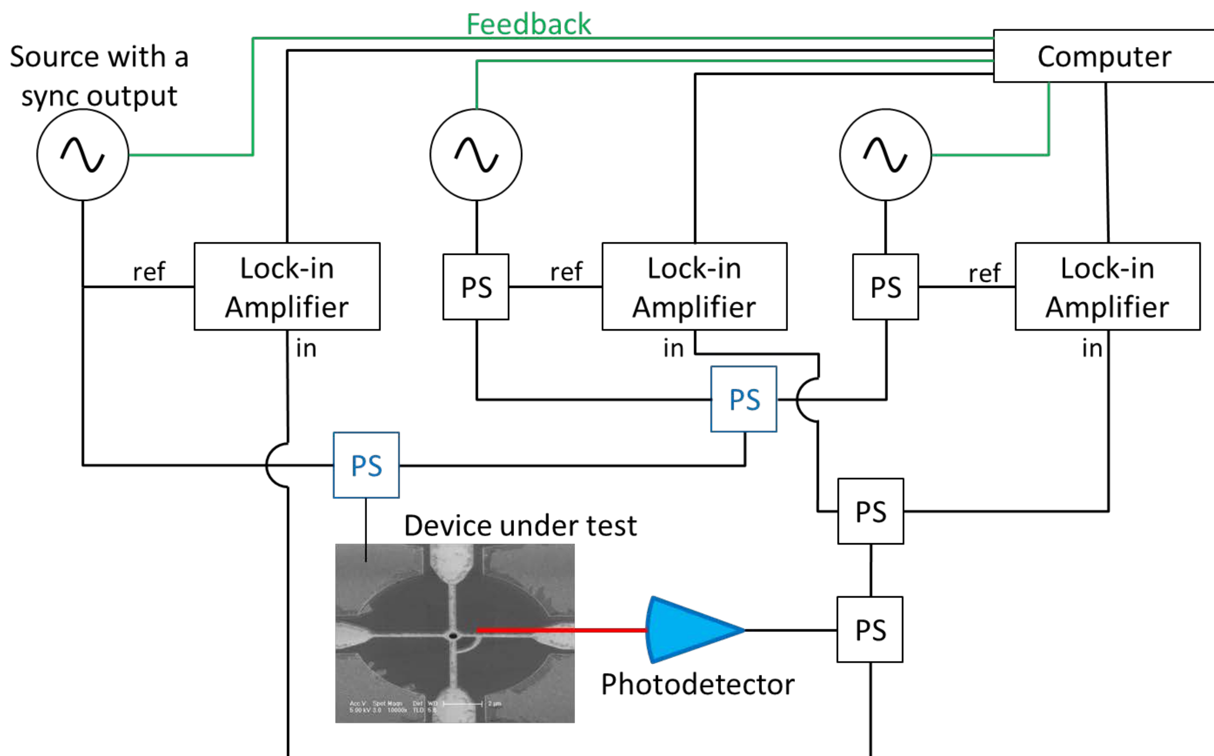

Figure 5.2: Schematic of the PLL setup for three modes. The blue power splitters are where they are used as power combiners.

Additionally we can adjust several parameters of the PLL system to improve our measurements. The first parameter is the timing of the system, which is characterized by two values, the lock-in time constant, τ_{LI}, and the sampling time, T_{sample}. The sampling time in general is taken to be about five times the lock-in time constant. τ_{LI} refers to the filter within the lock-in. Generally increasing this value will reduce the noise, but only up to a certain point as long term drifts will begin to set in. We also can adjust the filter value on the lock-in. Typically we choose a filter of 12 dB/octave. Within the LabView software, we can adjust the Y to ϕ conversion, a digital filter. This

is how fast or slow the PLL will adjust the frequency to shifts in the phase. Between all these parameters, we want to be able to minimize the noise processes in the system as well as maintain an efficient tracking time. Additionally, we want to optimize these parameters for the PLL loop time, explained below.

When a mass loading event occurs and the frequency downshifts, the entire time it takes from event to measurement by the system is known as the PLL loop time. Our goal is to match this loop time to the integration time corresponding to the minimum of the Allan deviation, as described in Section 2.3 to obtain the lowest mass sensitivity. Typically we first pick a τ_{LI} that minimizes the Allan deviation at the desired loop time. Then we adjust the Y to ϕ conversion such that a measurement will take about 20 data points from the occurrence of mass loading to reading the entire frequency jump.

5.3 Mass Sample Preparation

For the first generation of experiments, we utilized $40\ nm$ gold nanoparticles. These have a mass of $6.47 \times 10^{-19}\ kg$ or $389\ MDa$. To prepare the sample slides to mount into the chamber, we need to concentrate and dry the GNP sample. The GNP is purchased from Sigma-Aldrich as a colloidal suspension in a buffered salt solution. The first step is to perform a buffer exchange to replace the salt solution with deionized water (DI water). Our goal is to reduce the salt concentration by a factor of 1000. The purpose of this buffer exchange is to prevent any unwanted species from mass loading during the deposition process. To accomplish this, we spin down about $5\ mL$ of GNP solution in a

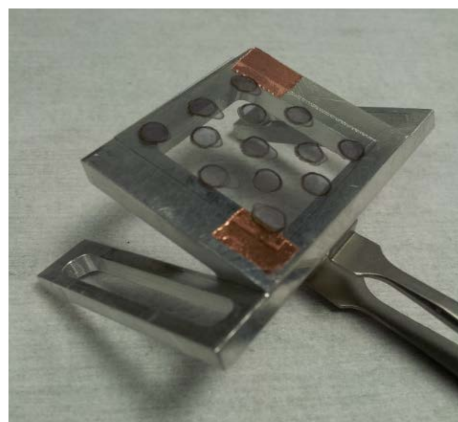

Figure 5.3: Picture of the sample slide where the GNP is deposited in a grid.

centrifuge to about $250\ \mu L$, then add in DI water back to $5\ mL$ and repeat several more times to wash out more salt each time. After this, we concentrate the GNP down to about $500\ \mu L$. Each of these centrifuge steps is done at $4500\ rpm$. This is enough material to create two slides.

The next step is to pipette the GNP onto a $1''$ square glass sample slide and then allow it to dry. To facilitate drying, we heat the sample slide at $80°C$ on a hot plate. Other techniques to speed up the drying process include vacuum drying or replacing the DI water with a solvent, such as isopropyl alcohol. The purpose of accelerating the drying is both to reduce the sample prep time as well as counteract what is known as the "coffee ring effect" which arises when droplets of solution are dried[4]. Figure 5.3 shows what a typical sample slide looks like. We notice that the edge of each dot is darker than the interior. This is due to the capillary flow that cause GNP to clump towards the edges of the liquid as it dries. The GNP solution can either be pipetted onto the sample slide in a grid like fashion or randomly. However after each layer, we must wait for it to dry before pipetting the next layer on. To be able to get sufficient covering, we typically pipette about ten layers.

From experimenting with the different procedures, heating the sample slide is the most efficient and most stable method of pipetting the GNP. Also, pipetting the GNP in a random fashion is easier for the desorption laser to produce an event because the particles are not concentrated in localized areas.

5.4 Mass Deposition Experiments

During the first test of the combined mass deposition/optical detection system, we only utilized one mode tracking to ensure that the system functions correctly. While we run the PLL frequency tracking on one mode, we scan and pulse the UV laser at a rate comparable to the PLL time.

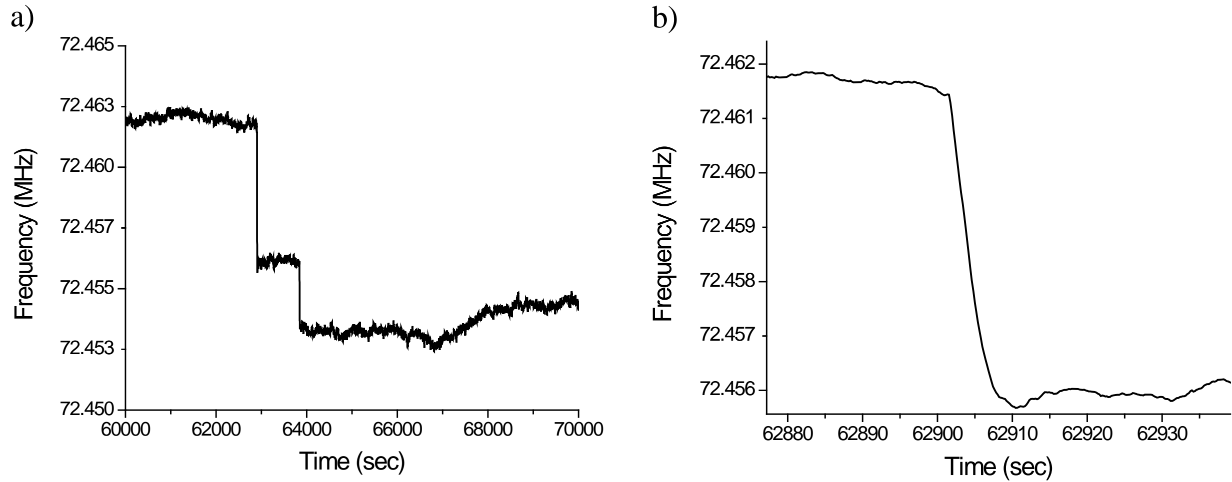

Figure 5.4: a) Data from first test run of setup tracking the first resonant mode. b) Zoomed in plot of the first frequency jump.

From the first test run, we see that we were able to resolve a few jumps. From 5.4b. we see that the PLL loop response time is about 5 seconds for the 5.5 kHz jump. This loop time and frequency shift seem reasonable. If we assume that the particle landed at the center ($\phi_{01} = 1, \phi_{11x} = \phi_{11y} = 0$), then we have an estimated mass corresponding to the mass of two 40 nm particles. However this is just an order of magnitude estimate to test the entire set up.

To confirm that we were able to successfully deposit GNP onto the device, we perform several experimental checks. The first check is simply to image the device for the presence of GNP under an SEM. A before and after image of the device is shown in Figure 5.5. On the left we see a fairly clean device, however in the right side image, we see distinct bright round spots. We believe that this corresponds to GNP due to the roundness and brightness of the particles.

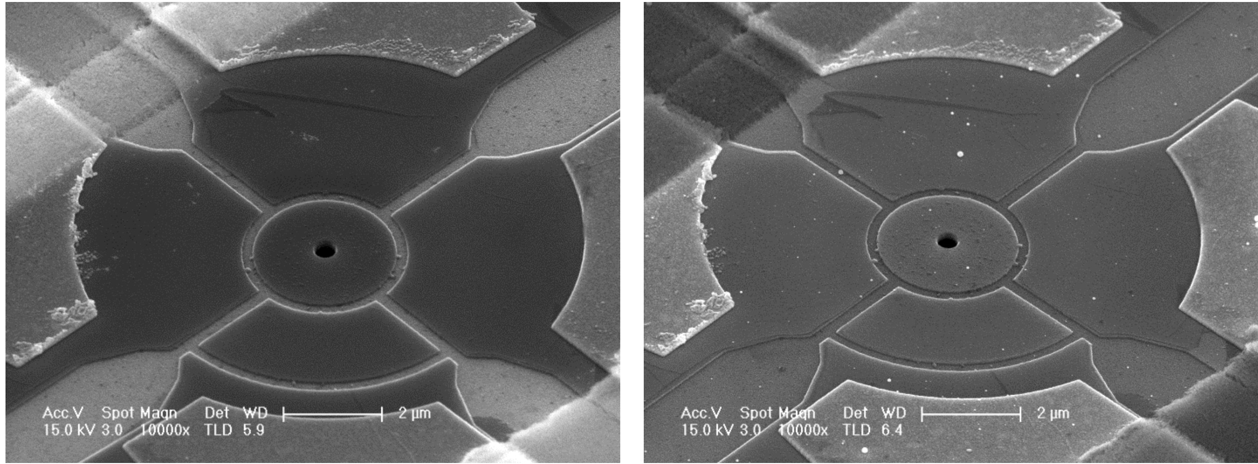

Figure 5.5: Before (left) and after (right) images of an AlN device under GNP mass deposition.

To confirm this, we perform energy dispersive x-ray spectroscopy (EDX) on both the device and these bright particles. EDX is a spectroscopy tool used to identify elements in a sample by focusing a beam of x-rays onto the sample. These x-rays then excite electrons in the sample into higher energy states. The excited electron can now either decay back into the ground state, releasing energy in the process, or can be ejected and another higher energy electron falls into the grounds state. In either case energy is released and this difference can be measured. Since each element has unique energy levels, we can identify the corresponding elements present in the sample.

Figure 5.6 shows the spectrum obtained for both the background and a particle. The black spectrum corresponds of the control measurement by focusing the x-ray beam on the surface of the device where there does not appear to be any GNP present. As expected, we can identify peaks at about 0.5 keV, 1.5 keV, 1.7 keV, and 2.3 keV. These correspond to oxygen, aluminum, silicon, and molybdenum, respectively. This is our expected background since all these elements are present within the device. When we focus the electron beam on a region with the GNP, we measure an extra peak at an energy of about 2.1 keV, which corresponds to the $M\alpha$ energy level of gold. This confirms the identity of the GNP. Table 5.1 summarizes these values.

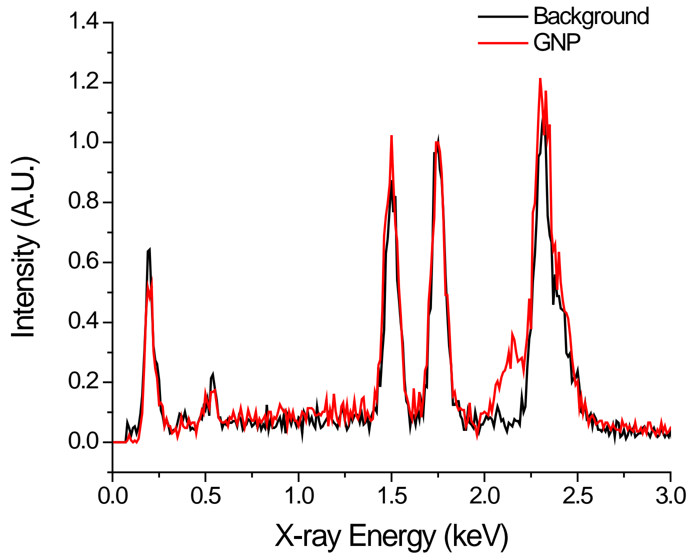

Figure 5.6: EDX of the device with and without GNP deposition.

Table 5.1: Summary of energy levels in O, Al, Si, Mo, and Au

Element	Energy (keV)	Level
Oxygen (O)	0.523	$K\alpha$
Aluminum (Al)	1.486	$K\alpha$
Silicon (Si)	1.740	$K\alpha$
Molybdenum (Mo)	2.293	$L\alpha$
Gold (Au)	2.120	$M\alpha$

From this we can now attempt to mass load while tracking three resonant modes. This is done with the same experimental setup, but with the full PLL structure described in Section 5.2. We also increase the GNP size to $80\ nm$. This is in order attempt to improve the visibility of the frequency shifts across all modes, since certain frequency shifts could be hidden within the frequency noise.

Data from this run is shown in Figure 5.7. We tracked the frequency for an extremely long period of time while rastering the UV laser over the GNP mass sample. We notice a distinct long term frequency shift of about $20 - 30\ kHz$ for each mode from a time of about 10000 seconds to 20000 seconds, however we were unable to resolve individual frequency jumps. We believe this large frequency shifts corresponds to multiple particles being deposited, but too rapidly for our PLL detection scheme to resolve. When a particle lands on the device, the PLL will begin

adjusting the measured frequency, however while the PLL is still adjusting, another particle is deposited and further shifts the frequency. This causes the data to be mixed between particle events. In addition, several other runs gave us similar results, where we see regions of large frequency shifts, however the flux rate was again too fast for us to resolve the shifts.

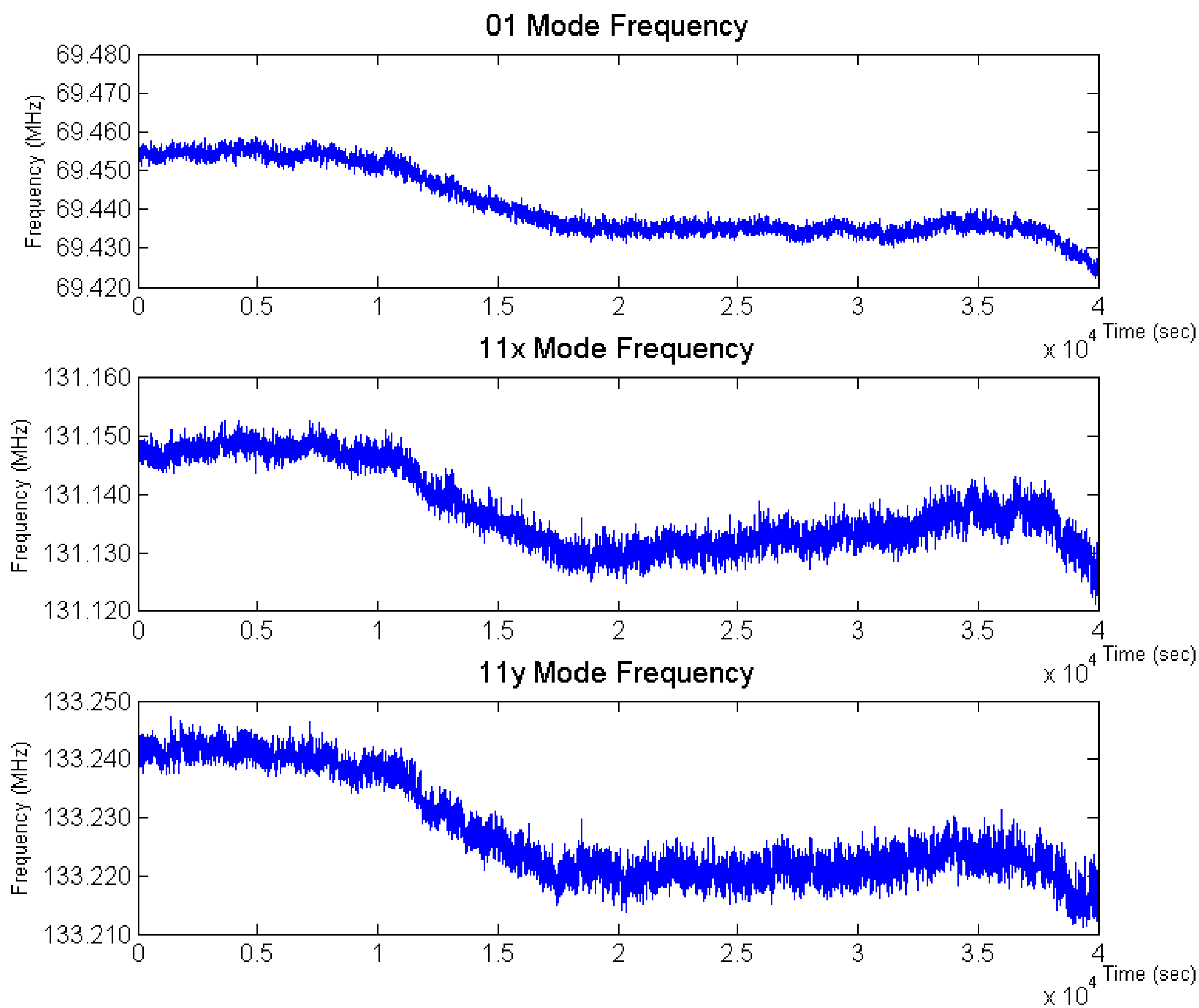

Figure 5.7: Frequency tracking data for the first three modes during mass deposition of 80 nm GNP.

Nonetheless, from this round of experiments, we were able to show that we can track the frequency shifts across all three modes and that we can mass deposit with our current setup.

From these scans, we were also able to back calculate the positions of the UV laser that corresponded to the downward frequency shift region. This would allow us to narrow down the scanning region of the UV laser to make the scan more efficient and allow us to scan the laser with finer resolution. By performing PLL scans with the order of X and Y motors swapped, we were able to identify a ¼” by ¼” region of the slide that seemed to correspond to the optimal location for mass deposition. Future experiments will most likely focus on this region of the slide. This also allows us to save GNP solution by creating the sample slide with material only in this region.

Chapter 6:

Conclusion

In conclusion, we have worked out the mathematical model for 2-dimensional mass spectrometry with NEMS circular membrane devices. From the simulations we see that the calculations should work. In addition we showed the improved capability of optical detection for this type of measurement by eliminating the background capacitive noise. Previous work within the group has shown that optical detection is advantageous for graphene measurements, so this experimental setup opens the door for mass spectrometry with graphene devices. We were also able to record preliminary data showing the ability for this setup to deposit particle onto the device as well as the ability for it to track up to three frequency modes of the device. Our preliminary data and investigation showed initial signs of mass deposition, however our flux rate and mass resolution needs to be improved.

For further work, we are interested in optimizing the setup. In particular we wish to improve the flux rate of the system. This can be done by better controlling the position of the laser or the rate of pulsing. Additionally we wish to improve the Allan deviation in order to improve the measurement. Also as briefly mentioned earlier, we wish to try out graphene devices for mass spectrometry due to their low device mass. We are also looking to measure higher modes to expand our multimode measurement to track four or five frequencies to improve our resolution.

Bibliography

1. Andersson, C-O. “Mass Spectrometric Studies on Amino Acid and Peptide Derivatives”. *Acta Chemica Scandivanica*. 1958 **12** 1353.
2. Beynon, J.H. “The Use of the Mass Spectrometer for the Indentification of Organic Compounds”. *Microchimica Acta*. 1956 **44** 437-453.
3. Bunch, J.S, *et al*. “Electromechanical Resonators from Graphene Sheets”. *Science*. 2007 **315** 490-493.
4. Deegan, R.D, *et al*. “Capillary Flow as the Cause of Ring Stains from Dried Liquid Drops”. *Nature*. 1997 **389** 827-829.
5. Deutsch, B.M, *et al*. “Non-degenerate Normal-mode Doublets in Vibrating Flat Circular Plates”. *American Journal of Physics*. 2004 **72**(2) 220-.
6. Dubois. M, P. Muralt. “Properties of Aluminum Nitride Thin Films for Piezoelectric Transducers and Microwave Filter Applications”. *Applied Physics Letters*. 1999 **74** 3032.
7. Ekinci, K.L, M.L. Roukes. “Nanoelectromechanical Systems”. *Review of Scientific Instruments*. 2005 **16** 061101.
8. Ekinci, K.L, Y.T. Yang, M.L. Roukes. “Ultimate Limits to Inertial Mass Sensing Based Upon Nanoelectromechanical Systems”. *Journal of Applied Physics*. 2004 **95** 5.
9. Ekinci, K.L. “Electromechanical Transducers at the Nanoscale: Actuation and Sensing of Motion in Nanoelectromechanical Systems (NEMS)”. *Small*. 2005 **1** 786-797.
10. Hanay, M.S. *Towards Single-Molecule Nanomechanical Mass Spectrometry.* PhD thesis, California Institute of Technology. 2011.

11. Hanay, M.S, *et al*. “Single-Protein Nanomechanical Mass Spectrometry in Real Time”. *Nature Nanotechnololgy*. 2012.
12. Karabacek, D.M, *et al*. “Diffraction of Evanescent Waves and Nanomechanical Displacement Detection”. *Optics Letters*. 2007 **32**(13) 1881-1883.
13. Karabalin, R.B, *et al*. “Piezoelectric Nanoelectromechanical Resonators Based on Aluminum Nitride Thin Films”. *Applied Physics Letters*. 2009 **95** 103111.
14. Kharrat, C, E. Colinet, A, Voda. “H∞ Loop Shaping Control for PLL-based Mechanical Resonance Tracking in NEMS Resonant Mass Sensors”. *IEEE Sensors*. 2008 1135-1138
15. Kouh, T, *et al*. “Diffraction Effects in Optical Interferometric Displacement Detection in Nanoelectromechanical Systems”. *Applied Physics Letters*. 2005 **86** 013106.
16. Li, M, *et al*. “Ultra-sensitive NEMS-based Cantilevers for Sensing, Scanned Probe and Very High-frequency Applications”. *Nature Nanotechnology*. 2007 **2** 114-120.
17. Lifshitz, R, M.C. Cross. “Nonlinear Dynamics of Nanomechanical and Micromechanical Resonators”. *Review of Nonlinear Dynamics and Complexity*. 2008.
18. Mallet, J.W. “On Aluminum Nitride, and the Action of Metallic Aluminum Upon Sodium Carbonate at High Temperature”. 1876.
19. Naik, A.K, *et al*. “Towards Single-molecule Nanomechanical Mass Spectrometry”. *Nature Nanotechnology*. 2009 **4** 445-450.
20. Peng, W, *et al*. “Laser-Induced Acoustic Desorption Mass Spectrometry of Single Bioparticles”. *Angewandte Chemie*. 2006 **45** 1423-1426.
21. Sridhar, S, D.T. Mook, A.H. Nayfeh. “Non-Linear Resonances in the Forced Responses of Plates, Part I: Symmetric Responses of Circular Plates” *Journal of Sound and Vibration*. 1975 **41**(3), 359-373.

22. Sridhar, S, D.T. Mook, A.H. Nayfeh. “Non-Linear Resonances in the Forced Responses of Plates, Part II: Asymmetric Responses of Circular Plates” *Journal of Sound and Vibration*. 1978 **59**(2), 159-170.

23. Taylor, K.M, C. Lenie. “Some Properties of Aluminum Nitride”. *Journal of Electrochemical Society*. 1960 **107**(4) 308-314.

24. Yang, Y.T, *et al*. “Zeptogram-scale Nanomechanical Mass Sensing”. *Nano Letters*. 2006 **6** 583-586.

25. Young, D.J, C.A. Zorma, M. Mehregany. “MEMS/NEMS Devices and Applications”. *Springer Handbook of Nanotechnology*. 2004 225-252.